High intensity impulsive loading by explosively accelerated granular matter

Anne Kyner, Kumar Dharmasena, Keith Williams*, Vikram Deshpande** and Haydn Wadley

Department of Materials Science and Engineering, University of Virginia, Charlottesville, Va 22903, USA

* Newtec Services, Edgefield, SC

** Engineering Department, Cambridge University, UK

Abstract

The mechanism by which a spherical shell of granular matter is accelerated by an internal explosion together with its subsequent loading of a high ductility, edge clamped steel plate are investigated by a combination of instrumented experimentation and particle-based simulation. By using a large spherical explosive charge to drive the expansion of a water saturated synthetic sand shell, it has been possible to create sand front impact speeds with a test plate that exceeded 1200 m/s. Direct observations of the evolution of the sand front were made using a pair of high speed video cameras, and revealed rapid initial acceleration of the sand followed by deceleration, and the formation of locally faster sand spikes. The pressure evolution and specific impulse during sand particle impact were measured using a Kolsky bar. A discrete particle-based numerical simulation method implemented in the IMPETUS Afea code was then used to simulate the impulse applied to the Kolsky bar and to model deformation of the plate. The simulation analyzed the interactions between the explosively accelerated high explosive, air, and sand particles and the shock fronts that propagated across each interface after detonation. The impulse applied to the test plate and its support structure were well reproduced by the simulation. The simulations also revealed significant dispersion of the sand, with some sand particles attaining radial velocities that were almost 50% higher than that of the main front, and identified the presence of (an experimentally unobservable) instability at the energetic material-wet sand interface. The deceleration of the sand with distance of propagation was found to be the result of momentum transferring collisions with the background air, resulting in the formation of a strong air shock ahead of the sand front. This processes resulted in the eventual transfer of all the sand momentum to the air and significantly influenced the dynamically changing topology of the sand-air interface. While the differential acceleration of the sand particles to form a dispersed front, and their deceleration by air drag were well modelled, the development of “sand spikes” at the main sand front-air interface were not resolved by the simulations.

Corresponding author: Haydn Wadley

Key words: fluid-structure interaction, particle-based simulation, dynamic deformation

1 Introduction

Soil can be accelerated to very high velocity by the detonation of a shallow buried explosive [1]. The impact of this soil against a nearby structure applies large impulsive loads resulting in inelastic deformations and even rupture of the structure [2, 3]. The experimental assessment of potential mitigation strategies can be a difficult, time-consuming challenge, especially as the severity of the impulsive load increases. The problem is further complicated because the transient deformations responsible for failure are very difficult to directly observe due to obscuration by the ejecta [4]. Numerical simulations provide a complementary means for investigating potential mitigation concepts, provided the physics of soil acceleration [5-7], its impact loading of the structure [8-11], and the structures dynamic mechanical response are properly captured. The study presented here uses a combination of instrumented experiment and particle-based simulation to investigate the dynamic loading and response of a model test structure following detonation of a spherically symmetric granular material encased test charge.

The detonation of an energetic material results in conversion of a solid or liquid material to its gaseous detonation products across a high-pressure detonation front that travels through the explosive at the energetic materials characteristic detonation velocity [12]. For a buried event, this detonation front eventually reaches the interface between the explosive and the surrounding granular media [13], and compresses it across a shock front that propagates away from the detonation at the granular media's shock velocity [3, 5, 10, 13]. This compressive shock eventually reaches the granular matter - air interface. The high acoustic impedance difference at this interface results in a strongly reflected (sign converted) tensile shock returning towards the detonation center [13]. To conserve momentum during this reflection, the granular medium is accelerated (spalled) from the reflecting surface with sometimes high velocity. The spalled ejecta travels from the surface, and eventually impacts a target leading to its impulse loading [3]. For some combinations of depth of burial and soil properties, the majority of the impulse that loads a nearby structure results from soil particle impact rather than the momentum transferred by the air shock or detonation products [13].

The impulse created during buried explosive tests at outdoor test ranges can be sensitive to the composition, moisture content, temperature, and degree of compaction of the foundation beneath the test charge [4, 14]. Many of these factors are difficult to control, and the resulting irreproducubility of such tests greatly complicates experimental assessments of mitigation strategies. Dharmasena et al. [15] recently developed an experimental set-up to controllably load test structures with explosively accelerated soil. In this approach, a suspended spherical explosive charge was encased by an annular shell of silica particles (synthetic sand) of known mass, particle size and shape, and water content. Detonation of explosive charges with a mass of 0.1 - 0.3 kg encased in 5 cm thick sand shells resulted in sand front velocities of 300-600 m/s [15-17]. While the deformation of structures tested this way are readily measured after testing, the dynamic interaction of the sand with the structure was much more difficult to monitor because of

obscuration by incident and reflected sand, and by escaping detonation products. Simulations do not suffer from such problems.

Several numerical techniques have been proposed to simulate the blast loading of structures [18-24]. The widely used LS-DYNA code [25] allows several different approaches to be used for blast modeling [23] including pure Lagrangian approaches, sequential Eulerian followed by Lagrangian simulations, and fully coupled Eulerian-Lagrangian simulations. Fully coupled simulation allows the blast loading and structural response to be simulated during dynamic deformation of the structure where fluid-structure interactions can be significant [23]. In this approach, the response of the soil to impulsive loading by the detonation event and the loads applied by the soil to the test structure are calculated using a soil constitutive model. Many empirical continuum soil models have been proposed for this purpose [7, 26, 27], but all require careful calibration [6, 14, 26], and causality between soil structure/composition and impulse loads is obscurred.

Deshpande et al. [5] proposed a soil constitutive model based upon a particle-particle contact mechanics analysis that defined interactions between soil particles. This granular model examined two regimes of particle interaction corresponding to the dispersed and high-density particle packing limits. For dispersed particles, typical of conditions during soil propagation through air, the model defined particle contact law was analogous to that for gas molecule collisions in the kinetic theory of gases. The high packing density limit corresponded to a regime of semi-permanent contacts dominated by particle deformation and friction, which is representative of conditions during impact of the particles with a structure. Related corpuscular simulations have begun to be used for explosive loading simulations [24, 28]. They use the discrete particle approach to model the momentum transfer via contact forces between particles and between particles and a structure. This approach uses different rigid, spherically symmetric particles to represent high explosive detonation products, the surrounding air, and the soil. The contact laws governing interactions between the various particles, and with a structure, result in contact forces that are used in a finite element analysis to predict dynamic structural response. This approach has recently been implemented in the IMPETUS Afea Solver [24], and several studies have begun to investigate the accuracy of predicted structural responses [17, 24, 28-30]. In these studies, the explosive charges were small (less than 0.5 kg), sand front velocities were usually comparable to the speed of sound in air, and the effects of momentum transfer from the soil to the surrounding air did not appear to be significant. In this regime, once the soil particle contact model parameters were established, the simulated responses were in good agreement with the experimental observations.

The present study investigates the acceleration and impact of sand particles created by a model explosive event that launched a dispersed sand front with velocities of more than 1,200 m/s, and explores the validity of particle-based simulations of the test. The study investigates the response of a 2.54 cm thick high ductility stainless steel edge clamped plate to loading by a spherical, water saturated (synthetic) sand encased, high explosive test charge whose center was suspended above

the center of the plate. The temporal evolution of pressure applied by the sand particles was measured by simultaneously stagnating the sand against the end of an instrumented Kolsky bar. A pair of high speed video cameras were also used to make a full observation of soil front fragmentation and propagation towards the structure. The IMPETUS Afea code was then used to analyze the impulse loading of the Kolsky bar and the plate, and to examine the dynamic response of the test structure to which the plate was attached. The combination of sand impulse measurement, observations of the sand front evolution, and the measured plate deflection then enabled identification of the important physical phenomena associated with high intensity impulsive loading by granular media, and an assessment to be made of the extent to which a particle-based code was able to analyze them.

2 Experimental Setup

A high intensity soil impact loading experiment was conducted at an outdoor testing facility operated by the NEWTEC Services Group, Inc. (Edgefield, SC). A schematic illustration of the test setup is shown in Figure 1, with additional details given in Figure 2. The test utilized a rigid platform to support a square edge clamped test plate. The detonation of a suspended high explosive sphere encased within a spherical annulus of water saturated synthetic sand provided the impulse loading. A 3.81 m long, strain gauge instrumented, maraging steel Kolsky bar system was used for measurement of the sand impact pressure and impulse applied at a location symmetrically equivalent to the center of the test plate.

2.1 Test platform

A test platform was designed to enable the testing of edge clamped square test plates, Figure 1. A square support base with an overall footprint of 122 cm x 122 cm was constructed using a single layer of cinder block laid down on a concrete pad. Several wooden beam layers were placed on the cinder block to raise the platform to a height that enabled unobstructed observation of the test. A 0.95 cm thick rubber mat was placed on the wooden supports to cushion impacts, and reduce damage to the support structure. The rest of the platform was then assembled by positioning a square picture frame constructed from welded, 15.3 cm deep, A-36 steel I-beams on the support structure. To avoid test plate shear-off near the test plate edge clamping, a 3.8 cm thick, 122 cm x 122 cm, A-36 steel support plate with an 80 cm x 80 cm square, center cutout was attached to the steel I-beam picture frame assembly, Figure 2. The test plate was then attached to the periphery of this support plate where its center 80 cm x 80 cm opening defined the span during test plate testing, Figure 2. This enabled the total length of the edge clamped region to be large enough that the pull-in stresses at the edge attachment location were maintained below the yield strength of the test plate, thereby avoiding otherwise difficult to analyze edge effects during the test [16, 17].

2.2 Test plate target

The test plate target consisted of a 2.54 cm thick, 132 cm x 132 cm, 304L grade stainless steel plate, Figure 3. The plate was supplied by Rolled Alloys, Inc. (Temperance, MI) and was tested in the (as received) hot rolled, annealed and pickled (HRAP) condition. Very large forces must be

supported at the gripped edges of the test sample. Furthermore, studies with square plates that utilized edge grips that extended above the top surface of the plate were found to create very significant local impulse amplification due to the reaction momentum created during upward redirection of soil [17]. To prevent plate pull-in at its gripped edges during center impact loading, while also avoiding out-of-plane sand reflection at the periphery of the structure, 5.1 cm wide, 2.54 cm thick, rectangular cross section 304 grade stainless steel bars were welded in a picture frame pattern along the four edges of the eventual underside of the test plate, Figure 3. To further strengthen the edge restraint system, a series of holes were drilled through the edges of the test plate and the picture frame to enable insertion of ~19 mm diameter, press-fitted tool steel dowel pins. This combination of welded and pinned bars robustly connected the 2.54 cm thick test plate to the picture frame support, Figure 3. This edge reinforced test plate was secured to the test platform with four 19 mm diameter, Grade 8 steel bolts located near the corners of the test plate, Figure 2.

2.3 Test charge design and assembly

A high explosive charge was suspended directly above the center of the test plate. The charge was constructed using two thin wall, acrylic plastic, concentric sphere assemblies with thicknesses ranging from 4.8 mm at the equator to 1.6 mm at the poles of each hemisphere. The concentric test charge was assembled by filling a 160 mm diameter, inner sphere with 3 kg of C-4 explosive [31]. A thin walled cylindrical plastic pipe with an internal diameter of 10 mm penetrated a pole of one of the hemispheres for subsequent placement of a detonator in contact with the explosive surface, Figure 4(a). The explosive sphere was then centered inside a 304 mm diameter, outer sphere with a carbon fiber reinforced polymer (CFRP) suspension rod passing through the center of both spheres for eventual positioning of the charge above the test plate. The outer sphere was again constructed from two hemispheres, each with a 3.8 cm flange around the equator which aided in the test charge assembly but resulted in a ledge around the sphere. The approximately 72 mm wide annular space between the two spheres was filled with 18.8 kg of glass microspheres with a diameter of 150-200 μm, Figure 4(b). Grade GL-0191 soda-lime glass spheres were obtained from Mo-Sci Corporation (Rolla, Missouri), and were identical to those used in previous studies by Hollomon et al. [29] and by Borvik et al. [24] for sand model calibration. Finally, 5.0 kg of water was added to fill the void spaces between the packed silica microspheres forming a water saturated model test “soil”, Figure 4(c). An instantaneous (0 ms delay) model SP/SM (12-0) detonator with a 3.5 m copper lead wire manufactured by Dyno Nodel Inc. (Salt Lake City, Utah) was inserted into the explosive through the plastic pipe just prior to testing.

To ensure that the center of the Kolsky bar and center of the test plate were subjected to similar impulsive loads, the orientation of the sphere was adjusted such that the detonator axis was at an angle of 45 degrees to both the test plate normal and the axis of the Kolsky bar. The center of the spherical charge was initially suspended 45 cm above the center of the top surface of the test plate and at the same standoff distance from the Kolsky bar end face. However, after the sphere was suspended, sufficient time elapsed during placement of the detonator for a small displacement of

the charge to occur. The actual standoff distances (shown in Figure 2) to the plate and Kolsky bar could be measured from the high speed camera images captured immediately before detonation. These measurements indicated the test charge was displaced 1.8 cm downward towards the plate and 3.5 cm further away from the Kolsky bar prior to the detonation. The actual standoff distance from the charge center to the end of the Kolsky bar was H_k = 48.5 cm. If the top surface of the plate is taken to lie in the X-Y coordinate plane with the X-axis parallel to the Kolsky bar and origin at the plate corner, the coordinates for the center of the test plate are located at X = 66 cm and Y = 66 cm. The actual location of the charge center above the plate was X = 69.5 cm and Y = 66 cm, and the standoff distance from the charge center to the plate surface was H_p = 43.2 cm.

2.4 The Kolsky bar

The pressure applied by impact of the water saturated sand was measured using a 2.54 cm diameter, 3.81 m long, age hardened C-350 grade, maraging steel Kolsky bar (Figure 1). Plastic bushings were placed around the Kolsky bar where it was attached to a series of pedestals to minimize energy leakage of the elastic modes of the Kolsky bar [32]. The end of the Kolsky bar was positioned so that a spherically expanding wet sand front reached the test target and the Kolsky bar almost simultaneously. Even though the charge had shifted slightly and was not equidistant to the test plate and end of the Kolsky bar, the Kolsky bar measurement still provided a quantitative measure of the pressure and impulse loading experienced near the center of the test plate. The simulation of its response provided a critical test of the validity of the numerical simulation approach. To minimize plastic deformation during impulsive loading, the maraging steel bar was aged before use at a temperature between 480 and 510°C for a period of 6 hours to achieve a Rockwell "C" scale hardness value of ~58 (equivalent to a tensile strength of ~2.07 GPa). Strain gauges were mounted on the Kolsky bar to enable the impact pressure to be measured, Figure 5. Two, T-rosette type strain gauges (Vishay Precision group, CEA-06-125UT-350), each with a pair of axial and transverse oriented strain gauge grid patterns, were adhesively bonded to the Kolsky bar, 0.5 m from the impact end, using Vishay AE-10 epoxy adhesive. The gauges were diametrically opposite to each other and were wired in a full-bridge Wheatstone bridge voltage measurement mode, Figure 5(a). A protective coating recommended for outdoor gauge installations (Vishay Gage Kote #5), was applied over the strain gauges and the fine lead wires.

Figure 5(b) shows the signal conditioning and digital signal acquisition arrangement used to record the strain gauge voltages. The output of the strain gauge circuit was fed through a 7 m long 8723 Multi-Conductor, Shielded Twisted Pair cable to a 1 MHz bandwidth amplifier (A.A. Lab Systems Ltd., G-3020) with an amplifier gain of 100. The output signal from the amplifier was then recorded with a digital oscilloscope (Tektronix, TPS2014) using a sampling rate of 1 MHz at 8-bit resolution. A total of 2500 digitized samples were recorded (a 2.5 ms record length). The recording of the signal was initiated by a trigger event created by the breaking of a wire attached to the outer surface of the polymer shell containing the synthetic sand. This resulted in a time delay of 40 μs between the beginning of detonation and the time at which the trigger wire was broken. To avoid confusion, the initial time t = 0 s is defined as the moment of detonation, and 40

μs has been added to the experimental Kolsky bar data in all the results to follow. For protection from the blast, the instrumentation was placed at the side of the Kolsky bar in a robust metal box and covered with sand bags.

The input-output voltage relationship for the full-bridge wired measurement circuit used here is given by,

$$\frac{V_0}{V_i} = \frac{GF(1+\nu)\varepsilon}{2+GF(1-\nu)\varepsilon} \qquad (1)$$

where GF = 2.15 is the gauge factor for the Vishay strain gauge, ε the axial strain in the Kolsky bar, ν = 0.28 the Poisson ratio of the bar material, V_i = 10 V the input excitation voltage, and V_o the measured output voltage. The axial strain deduced from the V_o/V_i ratio and equation (1) was then used with Hooke's Law and Young's modulus of the bar (E = 180.7 GPa), to determine the axial compressive stress (pressure) within the Kolsky bar. The transmitted specific impulse (units of kPa·s) was found by integration of the pressure waveform over time from t = 0 s defined as the initiation of detonation.

2.5 High speed video imaging

Two Vision Research Inc., Phantom V7.3 high speed cameras were positioned side by side in front of the test stand at ~20 m from the charge to enable the wet sand front to be observed after detonation of the charge. A plan view of the X-Y plane, Figure 6, shows the experimental set-up with the locations of the cameras (placed side by side). An expanded view of the test plate in the X-Y plane indicates the distances to the plate center and the charge center location from the edge of the test plate (measured with the cameras). To provide a reference for distance and velocity calculations, a 20 cm long section of the front end of the Kolsky bar, and the full width of 132 cm wide test plate front side were spray painted in white prior to the experiment. One camera provided a wide view of the entire event with a 640 x 480 pixel resolution and a 30 μs exposure time at 142 μs intervals. The second camera used a 512 x 256 resolution and 20 μs exposure time at 47 μs intervals to provide a magnified image of the test charge. These images were used to measure the sand front position. The cameras spatial resolution was reduced to allow the capture of more frames per second and therefore increase the temporal resolution. The higher magnification camera captured images that were 1.14 x 0.57 m^2 in area, with each pixel corresponding to 2.23 x 2.23 mm^2 area in the observation plane.

3 Simulation Methodology

The suspended charge test geometry was simulated using the IMPETUS Afea Solver [24]. This code employs a discrete particle based method using air, high explosive (HE), and soil particles. A particle contact interaction model is used to determine the interaction between these discrete particles while contact forces created by particle impact with the test structure are coupled with a finite element (FE) model of the test plate and support structure to determine dynamic

deformations. The approach considers only the translational degrees of freedom of the system. Particle rotation is not addressed, which is equivalent to ascribing an infinite angular moment of inertia to the particles. This discrete particle method used here was first described by Borvik et al. [23] and Olovsson et al. [28], and has been validated as an analysis tool for low soil velocity blast loading by several studies [17, 24, 29, 30]. Particle contact parameter calibration was performed by Borvik et al. [24] with data from an experimental study [15] using spherical, sand encapsulated, 150 g high explosive charges. The sand in those tests was identical to that used here.

The simulation model used the geometry of the experimental setup with a charge suspended over a 2.54 cm thick, edge gripped solid plate that was bolted at its four corners to a steel support plate placed on an I-beam picture frame base structure, Figure 7. A 3.81 m long Kolsky bar was placed 45 cm above the test plate to determine the predicted pressure and impulse loading. The spherical charge was constructed with an inner sphere of high explosive material surrounded by an outer annular region of wet sand particles contained within a 3 mm thick acrylic plastic shell of 152 mm radius. The ledge around the outer shell was not modeled as it appeared to have no effect on the loading of the Kolsky bar or test plate as a result of its inclination. The inner sphere was also confined in a 3 mm thick acrylic plastic shell with a radius of 80 mm. The inner sphere was filled with sufficient HE particles to represent a 3 kg charge with the properties of C-4. This concentric sphere charge was suspended in air at a vertical standoff distance of 43.2 cm from the center of the charge to the top of the solid plate. The horizontal standoff distance from the center of the charge to the front of the Kolsky bar was 48.5 cm. Both distances were consistent with those measured from the experimental high speed video images just prior to detonation. This data set the center of the charge at X = 69.5 cm, Y = 66 cm, and Z = 43.2 cm. The detonation point was defined at a 45 degree angle from the top center of the spherical charge and at the edge of the C-4, located on the opposite side of the Kolsky bar. One additional simulation test was performed with a second Kolsky bar positioned at the center of the test plate location (X = 66 cm, Y = 66 cm, and Z = 0 cm with the front of the Kolsky bar in the X-Y plane 45 cm below the center of the test charge). It confirmed that the impulse applied to both Kolsky bars (when each was placed at a 45 cm standoff distance from the test charge center) were the same, validating the assumption that radial expansion and loading are equivalent in these two directions, and confirming that the horizontal Kolsky bar could be used as a witness of the blast load near the center of the test plate.

3.1 Particle model

The air and HE particles used by the solver were modeled as rigid particles each representing many actual particles that transfer momentum via collisions. Following Olovson et. al. [28], particle interactions between air and HE particles were taken to be elastic, consistent with Maxwell's kinetic theory of gases [33]. In this approach, IMPETUS models the air particles as an ideal gas with density $\rho = 1.3$ kg/m^3, initial internal energy $E_0 = 253$ kJ/m^3, and a ratio of specific heats $\gamma = 1.4$ with initial directions and velocities distributed at the start of the simulation according to the Maxwell-Boltzmann distribution [29]. The IMPETUS code has several predefined HE particle options that have been calibrated by Borvik et al. [24] by iterative simulation of a standard

explosive filled pipe test. For the simulations reported here, the C-4 high explosive option was selected with predefined parameters of initial density ρ_0 = 1601 kg/m^3, initial internal energy E_0 = 8.7 GJ/m^3, ratio of heat capacities γ = 1.4, particle initial solid-fill fraction b = 0.35, and a detonation speed D = 8190 m/s. The explosion was initiated at the detonator location by releasing HE into motion at a relase time given by R/D where R was the radial distance from the point of detonation and D the detonation velocity [24].

The water saturated (wet) sand was modeled with a penalty based (soft-particle) inter-particle contact law governing the behavior of the soil particles [24]. This contact model comprised of a linear spring k, in parallel with a linear dashpot with a damping constant c, which were in series with a Coulomb friction component characterized by a coefficient of friction, μ. The values selected for the normal spring constant and the damping parameter govern the normal motion while a horizontal spring constant and the friction coefficient govern the tangential motions during inter-particle contact. The sand input parameter model was calibrated for 150-200 μm diameter, silica glass microspheres (density of 2700 kg/m^3) for both dry and water saturated (wet) sand. The dry sand fill fraction was 60% for the glass spheres with initial density ρ = 1620 kg/m^3. The solver, rather than directly modeling the water in the wet sand, accounts for water effects by modifying the sand particle contact friction, contact stiffness, and damping as proposed by Borvik et al. [24]. The wet sand was given an initial density ρ = 2020 kg/m^3. The calibrated wet sand parameters include the soil-soil particle contact stiffness k_0 = 4.0 GN/m, the soil-soil particle contact coefficient of friction μ = 0.0, and soil-soil particle damping coefficient ξ = 0.005.

To analyze the sand particle distribution, the sand particle density was calculated at specified time steps after detonation. The simulated volume was segmented into approximately 1 cm^3 volume rectangular cells in a radial direction of interest. The number of simulated sand particles in each cell was determined to calculate the simulation particle density, $(\frac{N}{cm^3})_i$ (number of particles/cm^3) where N is the number of sand particles in the segmented cell i. The sum of the particles in all cells was also calculated, $\sum_j(\frac{N}{cm^3})_j$. The particle density was then divided by the total number of simulated sand particles to calculate a particle probability density, $\frac{(\frac{N}{cm^3})_i}{\sum_j(\frac{N}{cm^3})_j}$.

A convergence study indicated the simulation converged at 2 million total particles divided (by the solver) into 803,849 air, 439,911 sand, and 756,240 HE particles. For the 2 million particle simulation results shown here, one simulated sand particle was equivalent to approximately 5,200 actual sand particles.

3.2 Finite Element model

A cross sectional view of the model and the suspended spherical charge with the model coordinate system defined is shown in Figure 7. The coordinate axis origin was located at the top front left corner of the test plate, shown in Figure 6. The 3.81 m long Kolsky bar was modeled using the IMPETUS Afea Solver finite element package as a series of four cylindrical parts each of diameter 2.54 cm merged together, using the merger option in the solver. A 2.54 cm length

cylindrical section located at the front of the bar was used to measure the impact force on the front of the Kolsky bar. The second cylindrical part was 47.86 cm in length and ended at the location of the strain gauges where the pressure was experimentally measured. The third part consisted of a 4 mm cylinder representing the region where strain gauges were located and was used to measure the bar pressure. The fourth cylindrical section covered the remaining length of the bar. The full bar model was constructed from 39,000 linear hexahedra elements with 43,248 nodes.

The 2.54 cm thick solid plate with in plane dimensions of 132 cm x 132 cm, was supported on a test platform consisting of a 3.8 cm thick support plate, with an 80 cm x 80 cm center opening on top of an I-beam picture frame structure. To clamp the edges of the plate securely to the test platform, an outer (5.1 cm wide and 2.54 cm thick) picture frame was merged to the solid 2.54 cm thick plate to represent the four rectangular bars that were welded and pin reinforced to the test plate. The bottom plane of the model was constrained in the X, Y, and Z directions using a fixed boundary condition. A mesh sensitivity analysis was performed to determine the number of elements needed for solution convergence. The final full model geometry, including the inner and outer spherical acrylic shells, test plate, test platform, attachment bolts, and the Kolsky bar, was meshed with a total of 44,284 elements; 288 linear pentahedra elements, 42,320 cubic, and 1,676 linear hexahedra elements with 129,432 nodes. The test plate used a more refined mesh than the support structure and the Kolsky bar to better observe the plate deflection during impulse loading. The full test plate with rectangular bars forming the picture frame edge consisted of 1,676 cubic hexahedra elements with 62,964 nodes.

3.2.1 Material models

The test plate, support frame, and Kolsky bar were all modeled as isotropic, Johnson-Cook materials. The IMPETUS Afea Solver uses the Johnson-Cook (J-C) constitutive model to calculate the von Mises flow stress defined by [29],

$$\sigma_y = \left(A + B\left((\varepsilon_{eff})^n\right)\right) \cdot \left(1 + C \ln\frac{\dot{\varepsilon}_{eff}}{\varepsilon_0}\right) \cdot \left(1 - \left(\frac{T - T_0}{T_m - T_0}\right)^m\right) \quad (2)$$

where A, B, n, C, and m are material constants and ε_{eff} is the effective plastic strain of the material. The strain hardening constant parameters are the initial yield strength A, the two hardening parameters B and n, the strain rate parameter ε_0, and the strain rate hardening parameter C. The J-C model also included the ambient temperature T_0, melting temperature T_m, and the thermal softening parameter m, for the material. The J-C model parameters for 304SS were reported by Dean et al. [34] and by Mori et al. [35] for annealed 304SS. For the A-36 steel constitutive model, the model parameters for ASTM-A36 were assumed [36]. The J-C parameters for 350 grade, maraging steel were taken from parameters for a similar VascoMax 300 alloy [37], assuming approximately equivalent material properties with an adjusted yield strength parameter for 350 grade steel. The reported value for the yield strength of 350-grade commercial maraging steel is 2.195 GPa with an ultimate tensile strength of 2.227 GPa [38]. The J-C parameters used with

Equation (2) are summarized in Table 1 for the three materials. There was no fracture of the test plate so a failure model for 304SS was not included in the simulation model.

Table 1. Material constants for 304SS, A-36 steel, and C-350 maraging steel.

Material	Density and elastic constants			Yield stress and strain hardening			Strain rate hardening		Temperature softening and adiabatic heating		
	ρ ($kg \cdot m^{-3}$)	E (GPa)	ν	A (MPa)	B (MPa)	n	C	ε_0 (s^{-1})	T_0 (K)	T_m (K)	m
304 SS	7900	200	0.3	310	1000	0.65	0.07	1.0	293	1673	1.0
A-36	7850	199	0.3	244	484	0.235	0.0165	0.0002	300	1790	1.03
C-350	7900	180.7	0.283	2195	9400	1.175	0.0046	1.0	300	1685	0.78

The acrylic polymer spherical shells used for both the inner shell (containing the HE) and the outer shell (containing the wet sand), were modeled using a linear elastic constitutive model with acrylic plastic values of density $\rho = 1180$ $kg \cdot m^{-3}$, Young's modulus E = 2.80 GPa, and Poisson's ratio $\nu = 0.37$. The failure criteria for the plastic model was set at an effective geometric strain of 10%. When elements in the geometric shell, reached the failure strain $\varepsilon_{fail} = 0.1$, they were eroded.

4 Sand Shell Expansion

4.1 High speed video observations

Figure 8 shows a sequence of images of the test charge recorded with the wide field of view camera following detonation. Both the white painted side of the test plate and 20 cm length end of the Kolsky bar can be seen. The t = 0 s image in Figure 8(a) corresponds to the moment of detonation. The image was used to confirm that the test charge was displaced to the right of the plate center by 3.5 ± 0.3 cm and downwards from the Kolsky bar center axis by 1.8 ± 0.3 cm, resulting in actual standoff distances (measured from the test charge center) to the plate $H_p = 43.2 \pm 0.3$ cm and to the Kolsky bar end $H_k = 48.5 \pm 0.3$ cm. The white sand front expanded almost isotropically with only a slight asymmetry in sand front shape. It can be seen to impact the test plate between the images shown in Figure 8(c) and (d) at approximately t = 290 μs, slightly before impact with the Kolsky bar; consistent with the reduced standoff distance to the plate surface. The lower part of Figure 8(f) shows that after impact with the test plate the sand front had flowed laterally over the plate surface and off the edges of the test plate. This sand had a small upward component of motion consistent with sand refection at an increasingly acute angle of impact near the plate periphery. Careful examination of the sand front images in Figure 8 indicates the presence of locally faster sand sand spikes (sometimes referred to as "fingering") similar to those observed by Holloman et. al. [29] for buried explosive events. Figure 8(e) shows a magnified region where the sand spikes/fingers are easily identified. The images in Figure 8(d) and (e) indicate significant (white) luminescence associated with the first sand finger impacts with various parts of the test plate and the Kolsky bar support structure. The additional mass of the acrylic

polymer ledges around the equator of the test charge can be seen to have locally slowed the sand front. Due to the inclination of the charge, this had no effect upon the front expansion towards the test plate or end of the Kolsky bar.

Figure 9, shows a similar sequence of images obtained with the higher magnification camera using the same definition of time as Figure 8. Figure 8(b) and Figure 9(b) indicate that the sand sphere had already begun to radially expand at t = 72 μs. By backward extrapolation, it is estimated that the sand front began its movement at t = 40 ± 20 μs, consistent with the propagation of an explosive detonation front with handbook velocity of 8040 m/s [31] across the 160 mm diameter charge (in t = 20 μs) followed by the propagation of a shock through the 72 mm thick annular sand shell at a velocity of 3600 m/s [39, 40]. The main sand front is indicated with a black dotted line in Figure 9(d), and shows the fast moving sand spikes ahead of this main front. The image sequence in Figure 9 shows the length of the sand front fingers increased with time consistent with a locally higher sand velocity. The images in Figure 9(f) indicate the observable tips of the sand fingers had advanced between 2 and 5 cm ahead of the main, sand front at 453 μs after detonation. Impact of the stretching sand with both the end of the Kolsky bar and the center of the test plate was therefore distributed over time. Examination of the high speed video also showed that the sand front developed a fractal like topology consisting of outwardly propagating sand cones that themselves became composed of smaller diameter cones as the sand radially expanded. Figure 10 shows the square region indicated in Figure 8(f) where conical features in the sand front decompose into smaller diameter cones over time.

A full analysis of the main sand front position was performed in the Kolsky bar horizontal direction by assuming the observed radial expansion was in the plane formed by the charge diameter and the axis of the Kolsky bar. Since it was difficult to identify a consistent front for the sand fingers, particularly early in the expansion process, only the main spherical sand front expansion (indicated by the black dotted line in Figure 9(d)) was measured. The experimentally deduced sand front location is plotted as solid black circles in Figure 11(a). Numerical differentiation of the main sand front leading edge position data gave a sand front velocity that is also shown as solid black circles in Figure 11(b). Error propagation analysis was used to estimate the uncertainty in sand front velocity [41], and resulted in a radial velocity error that decreased with time from ±96 m/s error for the earliest velocity estimate to ±15 m/s for the last data point.

It is evident from Figure 11(b) that the main sand front was rapidly accelerated to a maximum velocity of ~1200 m/s at 110 μs after detonation, and was followed thereafter by a slower, but prolonged period of deceleration. Given a measured standoff distance of 48.5 cm from charge center to the edge of Kolsky bar, and an initial outer sand sphere radius (including polymer shell thickness) of 15.2 cm, the distance from the front of the initially stationary annular sand shell to the front of the Kolsky bar was 33.3 cm. The distance of sand front propagation to the front surface of the target plate was 28 cm, since the standoff distance to the plate was 43.2 cm. Projection of these propagation distances on the position vs time plot, Figure 11(a), shows that the main sand front required a time of ~330 μs to reach the Kolsky bar and ~290 μs to reach the target plate.

Figure 11(b) indicates that at these instances, the main sand front's instantaneous velocity was beginning to decrease from its maximum value, and at impact with the Kolsky bar, the velocity was 1050 ± 44 m/s, and 1100 ± 50 m/s with the plate. The maximum estimated velocity of the fastest sand spike, v = 1470 m/s, shown in Figure 9(d), is indicated by the horizontal dotted black line in Figure 11(b). These sand spikes appear to be a manifestion of an interfacial instability that exists at high velocity granular matter-air interfaces [42-44].

4.2 Simulated sand front

The IMPETUS predicted HE and sand particle distributions for a sectional plane through the center of the plate and charge containing the axis of the Kolsky bar are shown in Figure 12. This view is analogous to that of the experimental time sequence images shown in Figure 9. Particle positions at the moment of detonation (t = 0 s) are shown in Figure 12(a). The subsequent simulated images show that the sand shell velocity was slightly asymmetric with the fastest sand propagating in the (southwest) direction; normal to the expanding detonation front. Significant sand velocity dispersion was present in all directions with some sand particles having travelled significantly further (at substantially higher velocity) than others. To help visualize this effect, Figure 12(e) shows the approximate location of the 1, 2 and 5% sand particle probability density contours at 310 μs after detonation (calculated using the procedure detailed in Section 3.1).

Figure 12(e) and (f) also show the initial interaction of the sand particles with the test plate surface. They indicate that sand impact with the test structure occurred slightly earlier than that with the end of the Kolsky bar consistent with experimental observations. The sand particles that made impact near the center of the test plate at zero obliquity suffered weak reflection, and accumulated in this region. This was consistent with the results of previous calculations of the impact of unconstrained sand slugs with rigid beams where the incident momentum of the sand slug was transferred to the test structure with little amplification by reflection [45, 46]. However, most particles did not behave in this manner. Instead, they made oblique impact with the plate, and were reflected along the plate surface with only a fraction of their incident momentum transferred to the plate. These sand particles eventually (not shown) left the surface as a thin sheet travelling radially outwards from the center of impact, consistent with the reflected sand identified in Figure *8*(f).

4.3 Sand acceleration

To better understand the sand shell acceleration process, Figure 13 shows sand and HE particle positions for the first 45 μs following detonator activation. The dotted white line in Figure 13(a) indicates the position of the detonation front at 10 μs after the initiation of detonation. The detonation shock front required 19.5 ± 0.5 μs to propagate the 160 mm diameter of the inner HE sphere and reach the southwestern edge of sand/HE interface (diametrically opposite the detonation location). This gives a detonation velocity of 8205 ± 210 m/s; consistent with the detonation velocity parameter, D = 8190 m/s, given as input to the solver, and is close to the handbook value for the detonation velocity of the C-4 explosive (8040 m/s) [31]. A compressive

shock wave was then launched into the 72 mm thick annular sand region, and can be seen as the line separating the darker (compressed) sand from the (original contrast) stationary sand, Figure 13(b)-(e). The approximate sand shock location is indicated by the black dashed line in Figure 13(b)-(e). The sand shock front reached the outer surface of the sand shell at t = 38.5 ± 0.5 μs, corresponding to a wet sand shock velocity of 3790 ± 100 m/s which is consistent with reported shock velocities in water saturated sands [40]. The acrylic shell (not shown in Figure 13) failed as the sand shock front reached the polymer shell inner boundary at t = 38.5 μs. At 45 μs after initiation of detonation, Figure 13(f), the sand shock had undergone reflection/sign conversion at the sand/acrylic interface and had begun to propagate back into the sand shell with concomitant spalling of the sand behind this release wave. The initial HE and sand front locations are indicated by dashed lines in Figure 13(f) to show how far the sand particles had been displaced from their initial locations at this time.

Detailed examination of the simulations showed that the radial distance of propagation of the sand particles within the sand shell was not uniform in the circumferential direction. To illustrate this, Figure 14 shows the displacement magnitude of the sand particles at t = 50 μs after detonation. Spikes at the green to blue interface can be seen within the inner region of the sand shell. They are consistent with the development of a shock induced interfacial instability whose conditions for initiation were recently analyzed by Kandan et al. [44] and shown to be a manifestation of a Richtmyer-Meskov type instability [44].

4.4 Sand layer stretching

Figure 12(c)-(f) showed the presence of a significant variation in the sand particle displacement, resulting in the development of a substantial sand particle density gradient. A significant fraction of sand was accelerated well ahead of the main sand front, while a trailing, much denser sand region existed directly in front of the expanding detonation products. To quantify the sand particle distribution, the simulated sand particle density was calculated (as detailed in Section 3.1) and is plotted as a function of distance from the test charge center in the Kolsky bar direction in Figure 15(a). It is evident from Figure 15(a) that at 102 μs after detonation, the density of sand particles was essentially zero beyond approximately 29 cm from the charge center. The sand particle density then increased behind the fast sand to reach a peak value (of about 5 simulated particles per cm^3) at a radial distance of ~15 cm from the charge center before falling very rapidly. During this period, the sand front expanded from an initial width of 7.2 cm, to 17 cm at 102 μs after detonation (and 24 cm at 182 μs and 26 cm at 208 μs after detonation). This was accompanied by a decrease of the sand particle density due to a combination of inverse square law spreading arising from growth of surface area of the sand shell, and radial stretching of the sand shell.

The sand probability density is shown for each time step in Figure 15(b). The horizontal lines shown on the figure correspond to particle probability densities of 1, 2 and 5%. Their intersection with the probability distributions in Figure 15(b) show the radial location of each probability density. These particle probability values were transposed as probability contours on the image

shown in Figure 12(e). The fastest sand (with a sand probability density of 1 to 2%) was consistent with the leading tips of the sand fingers (spikes) observed experimentally in Figure 9, and had advanced well ahead of the main front with a 5% particle probability density. The positions of the 1, 2 and 5% sand probability density contours are also overlaid on the experimental sand front location data obtained with the high speed camera in Figure 11(a). By comparing the simulated front locations at different time steps, it was also possible to calculate the sand probability density contour speed in the Kolsky bar direction, and this is overlaid on the experimentally estimated sand velocity in Figure 11(b). It can be seen that both the experimental and simulated sand fronts accelerated, reaching a maximum velocity between 80 and 150 μs after detonation. The fastest (1% probability density) sand observed in the simulations reached a peak velocity of almost 1800 m/s while the denser (5% probability density) sand reached a peak velocity of 1250 m/s, almost identical to that observed experimentally (1200 m/s). Since a significant particle density would be needed to reflect sufficient light into a camera pixel to be registered as light from the sand particles, it is suspected that the fastest sand spikes observed with the high speed video cameras (approximately 1500 m/s) corresponded to regions with a particle density greater than 1%.

4.5 Sand deceleration

There was a well-defined decay in sand front velocity after the peak velocity was attained in both the experiment and the simulation data, Figure 11(b). Examination of simulation results in which air particles are shown, Figure 16, indicates the development of an air shock front (a dense air layer) in front of the sand. A red dashed line in Figure 16(a) and (c) indicate the approximate location of this shock. The darker shade of blue indicates the presence of significantly higher air pressure behind the air shock front. This air shock had an estimated radial speed of approximately 1300 m/s. Examination of simulations conducted without air particles (Appendix A) showed no sand front velocity decay, indicating that the sand deceleration was a result of momentum-transferring collisions between sand and air particles associated with the formation of the air shock. Its presence in the experiment may also have contributed to the formation of sand fingers ahead of the main sand front; a hypothesis that is investigated by more appropriate shock instability analysis methods in a recent paper [44].

Kandan et al. [44] analysed the propagation of a sand front moving with a velocity V_s into air at atmospheric pressure, p_O and ambient temperature. The front generates an air shock wave as it pushed through air. The shock pressure p_f at the front of the slug was shown to be related to V_s by;

$$\frac{V_s}{a_0} = \frac{1}{\gamma}\left(\bar{p}_f - 1\right)\left[\frac{2\gamma}{\bar{p}_f(\gamma+1)+\gamma-1}\right]^{1/2}, \tag{3}$$

where $\bar{p}_f \equiv p_f/p_0$ is the normalized shock pressure and the air shock speed, c_f can be obtained from the ratio of specific heat, γ, the speed of sound, a_o for air and the normalized air shock pressure;

$$\frac{c_f}{a_0} = \left[\frac{\gamma - 1}{2\gamma} + \bar{p}_f \frac{\gamma + 1}{2\gamma}\right]^{1/2}, \quad (4)$$

The main sand front impacted the test plate with an incident velocity, V_s of ~1200 m/s, resulting in a shock pressure p_f ~ 2.3 MPa (23 times atmospheric pressure) and an shock speed of ~1520 m/s. This high air pressure loading (which scales with the sand front speed) on the expanding sand front results in an instability that casues breakdown of the front into an array of conical shaped protrusions [44]. We note that as momentum is progressively transferred to the air shock from the sand, the nature of test plate loading will be increasingly governed by the fluid structure interaction for an air shock [47-49].

5 Kolsky Bar Response

5.1 Experimental measurements

The time corrected (with t = 0 s corresponding to the moment of detonation) Kolsky bar pressure-time response is shown in Figure 17(a). Recall that observations at the strain gauge location were delayed by the time for a longitudinal elastic wave (with a speed of 4800 m/s for the C-350 maraging steel bar) to propagate 0.5 m along the bar (a time of 104 μs). The first (sign reversed) distal reflection from the end of the 3.81 m long Kolsky bar arrived 1.38 ms after the initial direct signal. The data from the Kolsky bar is therefore only plotted for the first 1 ms of recorded data and is not complicated by distal reflections. However, complex Pochhammer-Chree modes of the large diameter bar (used here to avoid buckling instability) resulted in a complex wavetrain that distorted the pressure response [50]. Figure 17(a) shows that the first compressive stress whose amplitude significantly exceeded the background noise was detected by the Kolsky bar strain gauges at ~420 μs after detonation. However, it was preceded by a sequence of very weak arrivals whose amplitude was no more than two times the background. The compressive stress associated with the first significant signal (at 420 μs) had an amplitude of less than 50 MPa, and was followed by similary weak signals until a large compressive pulse with a peak pressure of ~750 MPa arrived at 560 to 575 μs after detonation. Integration of the pressure-time curve gave the specific impulse transmitted to the bar, Figure 17(c). The impulse signal first began to rise very slowly between 350 and 400 μs, and was followed by small impulse jump of ~0.4 kPa·s between 410 and 445 μs. This was followed by a ~120 μs period of increasing impulse with an approximately constant impulse rate. The arrival of the large pressure pulse at approximately 575 μs after detonation caused a rapid rise in impulse to a final value of ~9.5 ± 1.5 kPa·s that persisted to the end of observation (1 ms). The plateau specific impulse is consistent with simple estimates of the impulse per unit area of 8.5 kPa.s calculated by distributing the momentum for 23.8 kg of water saturated sand accelerated to an average velocity of 1050 m/s evenly over a sphere of 48.5 cm radius (the standoff distance to the end of the Kolsky bar).

5.2 Simulated response

The axial stress due to the simulated sand impact with the end of the Kolsky bar was calculated from the simulated force-time signal at the strain gauge location and the cross sectional surface area of the Kolsky bar (5.07 cm^2), Figure 17(b). The impulse was then calculated as the time integral of the pressure-time response, and compares well with the experimental data in Figure 17(c). Four response regimes can be identified and are indicated in Figure 17(c); (i) an initial step in impulse arriving at the strain guage position at approximately 400 μs after detonation and persisting for 20-30 μs, (ii) a region of slowly rising impulse between approximately 430 to 560 μs, (iii) a rapidly rising impulse regime that began at 560 μs, and persisted for ~40 μs in the experiment and about twice this time in the simulation and (iv) a plateau region of no further increase in impulse that persisted from about 600 μs to beyond 1 ms. Again, careful examination of the response prior to region (i) reveals that the step in impulse was preceded by a weak, slowly rising impulse beginning approximately 360 μs after detonation.

The simulation can be used to calculate the impulse applied to the impacted end of the Kolsky bar by each particle type (air, HE, and sand). The impulse contribution to the signal at the strain guage location for each of the different particle types is shown in Figure 18. These sum to the specific impulse calculated at the strain guage location in Figure 17(c). The air shock initially impacted the end Kolsky bar at approximately 250 μs after detonation resulting in a signal reaching the strain gauges at ~355 μs. This appears to be responsible for a very weak, slowly rising impulse prior to the onset of region (i) step response. Figure 18 shows that the impulse from the air particle impacts leveled out at ~0.3 kPa·s at ~400 μs after detonation. The first (fastest) sand particles impacted the front of the Kolsky bar at around 300 μs after detonation, Figure 11, and their impulse signal began to be observed at the strain gauge at about 400 μs. This initial sand impact, when combined with the impulse from the air particles, led to the first jump in region (i) impulse. The region (ii) response in Figure 17(c) corresponded with a period of impact by low density, but high velocity sand while region (iii) corresponded to impact by the densiest sand front directly in front of the HE particles and ended at 600 ms after detonation. The HE particles began to impact the end of Kolsky bar at 470 μs with their associated impulse arriving at the strain gauge location at ~575 μs after detonation (as the last of the sand impulse was recorded). The HE particle impacts contributed very little additional impulse to the total response, consistent with a leveling out of impulse beyond 600 μs (the region (iv) response), Figure 17(c).

Further insight can be gained by examining the position of only the sand and HE particles that eventually impacted the end of the Kolsky bar, Figure 19. Radial stretching of the sand front with time (distance of propagation) can be clearly seen. The simulation sequence is analogous to that observed in a laboratory scale study of the impact of sand columns on a Kolsky bar [11]. The laboratory scale study also observed the sand column lengthening over time as it traveled through air. In both cases, this arose from progressive spallation of sand at the sand/air interface during reflection of a sand shock launched here by the detonation wave. Examination of Figure 19(b)-(d)

clearly shows that the highest velocity sand particles had advanced well ahead of the main front while lower velocity sand accumulated directly ahead of the detonation products. Careful analysis of the simulations indicated that the fastest (1% contour) sand, shown in Figure 12(e), reached the end of the Kolsky bar at approximately 280 μs after detonation, and was detected at the strain gauges at approximately 394 μs after detonation consistent with the simulation plot, Figure 17(c). However, Figure 18 showed the initial loading experienced on the bar was from the air shock particles at this time rather than the fastest moving sand. The 2% probability density contour arrived at the end of the Kolsky bar at ~300 μs. This is consistent with the first sand impact shown in Figure 18 and, coupled with the loading from the air particles, the existence of a region (i) response ~400 μs after detonation (Figure 17(c)).

The region (ii) response corresponds to the sand arrival with a probability density of ~5% or higher. The impulse loading from this sand reached the strain gauge location around 440 μs, consistent with a time during which the impulse was rising at a constant rate. This constant rate of loading persisted to 560 μs and was followed by a sharp jump in impulse to a plateau impulse of 9.2 kPa·s. This region (iii) response corresponds to the time at which the sand directly in front of the HE particles impacted the bar. This region of lower velocity but higher density sand remained just in front of the detonation products, Figure 19(f), and impacted the front of the Kolsky bar at about 450 μs after detonation and would therefore have begun to be detected at the strain gauges at ~555 μs after detonation. It is interesting to note that the arrival of the slower moving HE particles after the sand did not cause significant additional impulse to be transferred during region (iv); a consequence of efficient momentum transfer from lower mass HE particles to the denser sand.

There was good agreement between the measured (~9.5 ± 1.5 kPa·s) and simulated plateau impulse (9.2 kPa·s) results and the timing of the main features observed in the impulse waveform, Figure 17(c). It is also noted that while the simulations showed significant interactions between the air and sand particles, when simulations were performed without air particles, only a small difference in the impulse transferred to the Kolsky bar was observed. Figure 18 indicates that less than 10% of the impulse was transferred by air particles, and it is therefore concluded that the majority of the impulse loading occurred by the impact of sand.

6 Panel Deflections

6.1 Experimental observations

The deformed 2.54 cm thick, 304SS plate was sectioned through the point of maximum deflection at X = 71.3 cm and Y = 66.0 cm as shown in Figure 6. The deflection as a function of distance Y along the plate (with Y = 0 cm corresponding to the white painted near edge of the plate) is shown in Figure 20(b) for the full 132 cm length of the test plate. A permanent center deflection, U_{max} = 3.56 cm was measured near the midpoint of the section cut. This deflection profile was aligned with the cross-section image of the test plate, Figure 20(a), and lines

corresponding to the locations of the steel support frame and the I-beam picture frame are shown on the plot. The center of the test charge was located vertically above the Y = 66 cm line in Figure 20(b) at X = 71.3 cm which was also the location of maximum permanent deflection. There was no evidence of fracture observed in the plate after impact or of permament rotational deformations at the edge grips. However, the I-beam support structure did suffer plastic deformation (and in a subsequent test, the flange underwent partial rupture).

6.2 Simulated plate deformation

The calculated displacement response of the solid plate is shown in Figure 21. It shows the transient damped oscillatory displacement as the plate asymptotes to a steady state permanent displacement of 3.51 cm; a 1.4% difference to the experimentally measured maximum experimental displacement at X = 71.3 cm and Y = 66 cm. The simulated plate was then virtually sectioned along the Y axis at X = 71.3 cm (the same as the section in the experiment). This simulated permanent deflection profile is compared with the measured profile in Figure 20(b) and can be seen to be in excellent agreement with the measurement. The location of maximum simulated and measured deflection was slightly off the center of the plate due to the small drift in charge position prior to detonation.

Figure 22 shows the specific impulse distribution applied to the plate during the first 1 ms of loading. The maximum specific impulse was registered along the Y = 66 cm (center) axis of the test plate at a value of X = 71 cm; directly beneath the center of the charge. This maximum impulse has a value, I_t = 12.8 kPa·s; slightly higher than that incident upon the Kolsky bar because of the ~5 cm shorter standoff distance to the plate surface. The impulse then rapidly decayed with radial distance from this location falling to less than 1 kPa.s at the corners of the plate as a result of the longer standoff distance (inverse square law spreading of the sand and its deceleration by interaction with the air) and the oblique angle of incidence which reduces the fraction of particle momentum transferred to the plate surface.

A simulation was performed without the test plate present to determine the hydrodynamic pressure, $P = \rho v^2$ (where ρ is the sand density and v its velocity) and the incident impulse at the surface of the plate directly below the charge center. A sand particle detecting "sensor" with a cross sectional area of 0.04 x 0.04 m^2 was placed at the location of maximum impulse in Figure 22 and detected the passage of sand particles. The maximum calculated pressure was 560 MPa, similar to that observed experimentally. The incident impulse was calculated as I_o = 12.4 kPa·s resulting in a transmitted to incident impulse ratio I_t/I_o = 1.03, consistent with weak sand particle reflection [45].

Figure 23(a) shows the effective plastic strain on the top surface of the target plate, where the consequence of stretching of the plate during its impulsive loading can be seen along the diagonal lines connecting pairs of bolts. Figure 23(b) shows the effective plastic strain on the back face of the test plate where the highest strain was found to be located directly beneath the charge center and at stress concentrations near the bolt hole locations. Black dotted lines show the location of

the beam span defining support plate. Even though the loading to the plate was circularly symmetric in Figure 22, the strain distribution was strongly influenced by the square symmetry of the test plate and edge grip system.

The simulation methodology also enables detailed analysis of the response of the test frame during sand loading. Appendix B shows that significant elastic rotation of the support frame accompanied later stages of the the test. This resulted in a softened edge restraint. It also resulted in large inelastic deformations of some parts of the support structure indicating a need for a sturdier support structure for tests at this scale.

7 Concluding Remarks

A suspended spherical test charge consisting of a 3 kg high explosive sphere surrounded by an annular shell of 23.8 kg of water-saturated sand has been detonated above a 2.54 cm thick edge clamped stainless steel plate to explore the impulse transfer mechanisms and dynamic response of a ductile plate. A combination of high speed video and instrumented Kolsky bar measurements during the test were used in conjunction with particle-based simulations to analyze the impulse loading response of the 304 stainless steel plate by high velocity sand. The fidelity of the predicted pressure and impulse distributions for scenarios in which particle velocities exceeded 1200 m/s have been confirmed, and therefore enabled sand front propagation and spreading to be investigated at a fundamental level. It has also allowed the contributions to the total impulse from air shock, sand, and HE particles to be evaluated.

The study has shown that for the test geometry used here, 90% of the impulse was delivered to the test plate by the impact of sand particles. During propagation of the sand through background air, a strong air shock developed immediately in front of the sand. This air shock delivered the majority of the remaining impulse. Eventual impact of the detonation product impacts was responsible for almost no impulse transfer for the test geometry investigated here. The highest velocity sand particles acquired their momentum by spallation from the outer surface of the sand shell during reflection of a compressive sand shock front initiated by a detonation front that crossed the HE charge. The experimental study showed that this fast sand was distributed in sand spikes (fingers) whose tip speeds significantly exceeded that of the main sand front. However, the majority of the impulse was carried by a denser sand front that was driven from the rear by repeated collsions with expanding HE particles. The main sand front was accelerated to a velocity of ~1200 m/s during the first 130 μs of the event, but then began to decelerate. Simulations conducted with and without the presence of background air particles showed that the decleration resulted from momentum transfer from sand to air particles. The impact of the sand particles with the plate resulted in little outward reflection and therefore transferred little more than the incident momentum for zero obliquity impacts directly beneath the charge.

The IMPETUS solver was also used to simulate the structural response of the I-beam frame support structure used for the test. The simulation identified a region on the I-beam flange where very large localized plastic strains were developed during rotation of the gripping system which

corresponded with the location of the support structure rupture during a subsequent test. The solver was therefore found to be well suited for the engineering level design of impulsive resistant structures. While the simulations reproduced the impulse transfer from the detonation particles to the test plate well, they failed to provide insight into shock induced instabilities at the sand/HE and sand/air interfaces, or to capture the fractal-like evolution of the sand front topology, or the formation of sand spikes.

We note that the test conducted here was an example of a more general problem. During detonation, the release of the chemical (stored) energy of an energetic material creates an expanding shell of detonation products. While in any direction the detonation product momentum is high, the principle of conservation of momentum requires its integral about the charge center to be zero. Over time, the detonation product momentum in any direction is fully transferred to the sand shell, causing its rapid acceleration to a maximum value (dictated by detonation product momentum divided by the sand mass). For the test conducted here, most of the impulse was transferred to the structure by sand whose speed was near this maximum value. However, over time (or distance of propagation), the sand eventually transfers all its momentum to the surrounding air, and at large standoff distances, loading of a structure then occurs by air shock reflection. In this case, the impulse is sensitive to the air shock pressure created during the sand front expansion. Furthermore, because of inverse square law spreading, the transferred momentum, to a small area structure is likely to be low.

Acknowledgements

This research was funded by the Defense Advanced Research Projects Agency (DARPA) under grant number W91CRB-11-1-0005 (Program manager, Dr. J. Goldwasser).

Appendices

Appendix A

Simulations were run in the IMPUTUS Afea Solver with and without air particles to understand the effects of the air particles in the simulation, and how these particles effect the sand particle propogation. Figure A1 shows snapshots of a contour plot of the radial sand speed for a simulation with air particles present (left) and without air particles (right) at equivalent times. Figure A1(a) shows the fastest moving (red) sand particles in both simulations travelled in the south-west direction (direction of detonation). However, there was a higher fraction of fast sand particles in the airless simulation. As the sand expanded over time, Figure A1(b)-(d), the radial sand speed of the simulations conducted with air particles decreased (less red particles) while in the airless simulation the sand speed appears to have been less affected. To quantify these differences, Figure A2 shows the maximum radial sand speed for the fastest sand particles in both simulations. The two plots show that after almost instaneously acquiring a maximum speed at around ~40 μs after detonation, the particle speed in the airless simulation remained

constant while that with air reached a maximum velocity at between 80-150 μs after detonations and was followed by a prolonged deceleration, consistent with momentum transfer to the air.

Appendix B

Simulations of the test have revealed that shortly after sand impact with the test plate had been completed, the I-beam and support frame of the test facility was inelastically bent and suffered substantial rotation. Figure B1(a) shows the edge of the test plate connected to the A-36 grade steel support plate and I-beam flange of the test facilty structure. Figure B1(b) shows the deformed geometry at 2.2 ms after detonation. This corresponded to the time required for the support plate to reach its maximum rotation (of about 5 degrees) from the initial edge orientation. The maximum effective stress on the I-beam support frame predicted by the simulation was 535 MPa. Figure B2(a) shows the time dependent displacement of three nodes located on the test plate, the support plate, and the I-beam picture frame, Figure B1(b). The maximum displacement of node 22570 on the I-beam picture frame was 7.3 mm with permanent deformation of 3.8 mm and the permanent deformation of the support plate (node 20100) was 6.1 mm. Figure B2(b) shows the corresponding angle of rotation at these nodes as the support frame rotated and bent after impact. This rotation of the I-beam support frame resulted in development of a slightly more compliant edge restraint during the period of test plate oscillation, Figure 21.

In subsequent tests using a higher impulse loading, the I-beam flange near the corner of the picture frame support (parallel to the edge of the frame) ruptured, Figure B3(b). Figure B3(a) shows the effective plastic strain on the meshed I-beam for the loading condition used here at 5 ms after detonation. This area of maximum strain coincided with that of rupture and was consistent with the location of the point of rotation of the I-beam, Figure B3(b).

References

[1] J. Attwood, S. Khaderi, K. Karthikeyan, N. Fleck, H. Wadley, V. Deshpande, The out-of-plane compressive response of Dyneema® composites, Journal of the Mechanics and Physics of Solids, 70 (2014) 200-226.
[2] T. Ngo, P. Mendis, A. Gupta, J. Ramsay, Blast loading and blast effects on structures–an overview, Electronic Journal of Structural Engineering, 7 (2007) 76-91.
[3] A. Ramasamy, A.-M. Hill, A. Hepper, A.M. Bull, J. Clasper, Blast mines: physics, injury mechanisms and vehicle protection, Journal of the Royal Army Medical Corps, 155 (2009) 258-264.
[4] S.L. Hlady, Effect of soil parameters on landmine blast, in: 18th International symposium on the Military Aspects of Blast and Shock (Bad Reichenhall, Germany, 2004.
[5] V. Deshpande, R. McMeeking, H. Wadley, A. Evans, Constitutive model for predicting dynamic interactions between soil ejecta and structural panels, Journal of the Mechanics and Physics of Solids, 57 (2009) 1139-1164.
[6] Z. Wang, Y. Lu, Numerical analysis on dynamic deformation mechanism of soils under blast loading, Soil Dynamics and Earthquake Engineering, 23 (2003) 705-714.
[7] Z. Wang, H. Hao, Y. Lu, A three-phase soil model for simulating stress wave propagation due to blast loading, International Journal for Numerical and Analytical Methods in Geomechanics, 28 (2004) 33-56.
[8] D. Fox, X. Huang, D. Jung, W. Fourney, U. Leiste, J. Lee, The response of small scale rigid targets to shallow buried explosive detonations, International journal of impact engineering, 38 (2011) 882-891.
[9] E.G. Pickering, S.C.K. Yuen, G. Nurick, P. Haw, The response of quadrangular plates to buried charges, International journal of impact engineering, 49 (2012) 103-114.
[10] A. Neuberger, S. Peles, D. Rittel, Scaling the response of circular plates subjected to large and close-range spherical explosions. Part II: buried charges, International journal of impact engineering, 34 (2007) 874-882.
[11] S. Park, T. Uth, N. Fleck, H. Wadley, V. Deshpande, Sand column impact onto a Kolsky pressure bar, International journal of impact engineering, 62 (2013) 229-242.
[12] J. Akhavan, The chemistry of explosives, Royal Society of Chemistry, 2004.
[13] D.M. Bergeron, R. Walker, C. Coffey, Detonation of 100-gram Anti-personnel Mine Surrogate Charges in Sand, a Test Case for Computer Code Validation, National Defence, Defence Research Establishment Suffield, 1998.
[14] M. Grujicic, B. Pandurangan, R. Qiao, B. Cheeseman, W. Roy, R. Skaggs, R. Gupta, Parameterization of the porous-material model for sand with different levels of water saturation, Soil Dynamics and Earthquake Engineering, 28 (2008) 20-35.
[15] K.P. Dharmasena, H.N. Wadley, T. Liu, V.S. Deshpande, The dynamic response of edge clamped plates loaded by spherically expanding sand shells, International journal of impact engineering, 62 (2013) 182-195.
[16] J. Rimoli, B. Talamini, J. Wetzel, K. Dharmasena, R. Radovitzky, H. Wadley, Wet-sand impulse loading of metallic plates and corrugated core sandwich panels, International journal of impact engineering, 38 (2011) 837-848.
[17] H.N. Wadley, T. Børvik, L. Olovsson, J.J. Wetzel, K.P. Dharmasena, O.S. Hopperstad, V. Deshpande, J.W. Hutchinson, Deformation and fracture of impulsively loaded sandwich panels, Journal of the Mechanics and Physics of Solids, 61 (2013) 674-699.
[18] G.I. Kerley, Numerical modeling of buried mine explosions, in, DTIC Document, 2001.
[19] J. Wang, Simulation of landmine explosion using LS-DYNA3D software: benchmark work of simulation of explosion in soil and air, in, DTIC Document, 2001.

[20] J.D. Baum, E. Mestreau, H. Luo, R. Löhner, D. Pelessone, M.E. Giltrud, J.K. Gran, Modeling of near-field blast wave evolution, in: Collection of Technical Papers-44th AIAA Aerospace Sciences Meeting, 2006, pp. 2310-2320.
[21] Z. Wang, Y. Lu, H. Hao, K. Chong, A full coupled numerical analysis approach for buried structures subjected to subsurface blast, Computers & Structures, 83 (2005) 339-356.
[22] A.D. Gupta, Modeling and Analysis of a 3-D Asymmetric Mine-Soil-Hull Floor Interaction Problems with Mine Buried in Dry and Wet Sand, in, DTIC Document, 2001.
[23] T. Børvik, A. Hanssen, M. Langseth, L. Olovsson, Response of structures to planar blast loads–A finite element engineering approach, Computers & Structures, 87 (2009) 507-520.
[24] T. Børvik, L. Olovsson, A. Hanssen, K. Dharmasena, H. Hansson, H. Wadley, A discrete particle approach to simulate the combined effect of blast and sand impact loading of steel plates, Journal of the Mechanics and Physics of Solids, 59 (2011) 940-958.
[25] LSTC, LS-DYNA Keyword User's Manual, Version 971. Livermore Software Technology Corporation, (2007).
[26] L. Laine, A. Sandvik, Derivation of mechanical properties for sand, in: Proceedings of the 4th Asia-Pacific Conference on Shock and impact loads on structures, CI-Premier PTE LTD, Singapore, ANSYS Inc., 2001, pp. 368.
[27] D.C. Drucker, W. Prager, Soil mechanics and plastic analysis or limit design, Quarterly of applied mathematics, 10 (1952) 157-165.
[28] L. Olovsson, A.G. Hanssen, T. Børvik, M. Langseth, A particle-based approach to close-range blast loading, European Journal of Mechanics - A/Solids, 29 (2010) 1-6.
[29] R.L. Holloman, V. Deshpande, H.N.G. Wadley, Impulse transfer during sand impact with a solid block, International journal of impact engineering, 76 (2015) 98-117.
[30] R.L. Holloman, V. Deshpande, H.N.G. Wadley, Impulse transfer during sand impact with a cellular structure, International journal of impact engineering, 82 (2015) 36-58.
[31] M. Explosives, Department of the Army Technical Manual, in, TM 9-1300-214, September, 1984.
[32] J.A. Simmons, E. Drescher-Krasicka, H. Wadley, Leaky axisymmetric modes in infinite clad rods. I, The Journal of the Acoustical Society of America, 92 (1992) 1061-1090.
[33] J.C. Maxwell, Illustrations of the dynamical theory of gases., The London, Edinburgh, and Dublin Philosophical Magazine and Journal of Science, 19 (1860) 19-32.
[34] J. Dean, C. Dunleavy, P. Brown, T. Clyne, Energy absorption during projectile perforation of thin steel plates and the kinetic energy of ejected fragments, International journal of impact engineering, 36 (2009) 1250-1258.
[35] L. Mori, S. Lee, Z. Xue, A. Vaziri, D. Queheillalt, K. Dharmasena, H. Wadley, J. Hutchinson, H. Espinosa, Deformation and fracture modes of sandwich structures subjected to underwater impulsive loads, Journal of mechanics of materials and structures, 2 (2007) 1981-2006.
[36] E.L. Guzas, C.J. Earls, Simulating blast effects on steel beam-column members: Methods, Computers & Structures, 89 (2011) 2133-2148.
[37] J.D. Cinnamon, A.N. Palazotto, Z. Kennan, Material characterization and development of a constitutive relationship for hypervelocity impact of 1080 Steel and VascoMax 300, International journal of impact engineering, 33 (2006) 180-189.
[38] U.K. Viswanathan, R. Kishore, M.K. Asundi, Effect of thermal cycling on the mechanical properties of 350-grade maraging steel, MMTA, 27 (1996) 757-761.
[39] M. Prasad, M. Zimmer, P. Berge, B. Bonner, Laboratory measurements of velocity and attenuation in sediments, University of California, Lawrence Livermore National Laboratory, Report, 205155 (2004).
[40] D. Chapman, K. Tsembelis, W. Proud, The behavior of water saturated sand under shock-loading, in: Proceedings of the 2006 SEM Annual Conference and Exposition on Experimental and applied mechanics, 2006, pp. 834-840.

[41] J.R. Taylor, Error Analysis: The study of uncertainties in physical measurements, Sausalito: University Science Book, (1997).
[42] V. Rodriguez, R. Saurel, G. Jourdan, L. Houas, External front instabilities induced by a shocked particle ring, Physical Review E, 90 (2014) 043013.
[43] L.C. Taylor, W.L. Fourney, D.P. Lathrop, Surface Instabilities from Buried Explosives, in, DTIC Document, 2009.
[44] K. Kandan, S. Khaderi, H.N.G. Wadley, V.S. Deshpande, Instabilities in shock loaded granular media, In progress, (2016).
[45] S. Pingle, N. Fleck, H. Wadley, V. Deshpande, Discrete element calculations of the impact of a sand column against rigid structures, International journal of impact engineering, 45 (2012) 74-89.
[46] T. Liu, N. Fleck, H. Wadley, V. Deshpande, The impact of sand slugs against beams and plates: Coupled discrete particle/finite element simulations, Journal of the Mechanics and Physics of Solids, 61 (2013) 1798-1821.
[47] A. Vaziri, J.W. Hutchinson, Metal sandwich plates subject to intense air shocks, International Journal of Solids and Structures, 44 (2007) 2021-2035.
[48] N. Kambouchev, L. Noels, R. Radovitzky, Nonlinear compressibility effects in fluid-structure interaction and their implications on the air-blast loading of structures, Journal of Applied Physics, 100 (2006) 063519.
[49] K.P. Dharmasena, H.N. Wadley, K. Williams, Z. Xue, J.W. Hutchinson, Response of metallic pyramidal lattice core sandwich panels to high intensity impulsive loading in air, International journal of impact engineering, 38 (2011) 275-289.
[50] R. Davies, A critical study of the Hopkinson pressure bar, Philosophical Transactions of the Royal Society of London A: Mathematical, Physical and Engineering Sciences, 240 (1948) 375-457.

Figure Captions

Figure 1. Schematic illustration of the test geometry. A spherical test charge was suspended a distance H over the center of an edge clamped test structure with a Kolsky bar positioned a similar distance from the center of the charge. A detonator was placed at a position that bisected the directions between the charge center and the test plate and charge center and the Kolsky bar so that the soil impact with the center of the plate and the face of the Kolsky bar would be similar.

Figure 2. Schematic illustration of edge constrained test panel geometry, the location of the Kolsky bar (including its strain gauge location), and the test charge geometry and position at the instant of detonation.

Figure 3. Construction of the test plate with the welded frame used for attachment to the test stand. Steel dowel pins were press fitted to strengthen the welded connection between the test plate and the four rectangular bars.

Figure 4. The geometry and procedure used to assemble the spherical test charge and concentric shell of water-saturated sand.

Figure 5. (a) The strain gage sensor arrangement on the instrumented Kolsky bar. (b) Shows the signal conditioning and digital data recording arrangement. The trigger signal used to begin digital data recording was initiated by rupture of a break wire attached to the outer shell of the test charge.

Figure 6. Plan view of the X-Y plane showing camera locations. An expanded view of the test charge and plate shows the plate center, the charge center at detonation, and the point of maxiumum plate deflection (X = 71.3 cm and Y = 66.0 cm) after the event. The location of the section cut used to obtain a plate deflection profile is also shown. The origin of the coordinate system used for the study was at the front (lower) left corner of the test plate.

Figure 7. A cross-section through the mid-plane of the FE model geometry used for the IMPETUS Afea discrete particle based simulation. The coordinate axis origin was located at the front left corner of the top of the test plate (out of the plane of this figure) as shown in Figure 6.

Figure 8. Sand front propagation observed with the wide-angle video camera; (a) t = 0 s (instant of detonation), (b) t = 72 μs (c) t = 215 μs, (d) t = 358 μs, (e) t = 643 μs, (f) = 1.5 ms. The distance from charge center to the test plate, H_p = 43.2 cm and to the Kolsky bar, H_k = 48.5 cm. (e) Shows a magnified region of the outermost sand front and the developed sand spikes/fingers. The white box in (f) indicates the region observed in Figure 10.

Figure 9. Images of the sand using the higher spatial resolution high speed camera at times (a) t = 0 s (instant of detonation), (b) t = 72 μs, (c) t = 120 μs, (d) t = 168 μs, (e) t = 310 μs, and (f) = 453 μs. The sand progression towards the Kolsky bar, the main sand front expansion, and the sand fingering effect can be seen in (d).

Figure 10. Expanded square region of sand front expansion from Figure *8*(f) at increasing time to show conical sections developing.

Figure 11. (a) Experimental and IMPETUS Afea predicted sand front position measured in the Kolsky bar direction (horizontal X direction) and (b) sand front velocity vs time after detonation. The velocity of the fastest experimentally observable sand spike (finger) is also indicated on (b). The estimated time for the sand to reach both the Kolsky bar and test plate are also shown.

Figure 12. IMPETUS Afea predicted (tan colored) sand front positions from time t = 0 s corresponding to the instant of detonation. The position of the (red) HE particles is also shown. Sand particle probability density contours are identified in (e) showing that some high-speed sand had travelled much further than the main sand front. Air particles have been hidden in these results.

Figure 13. A simulation sequence following detonation showing propagation of the detonation front through the HE and the compressive shock front through the annular wet sand shell. (f) Indicates the distance the sand and HE particles were displaced from their initial locations at t = 45 μs after initiation of detonation.

Figure 14. Sand particle shell with color contours corresponding to the magnitude of the particle displacement at t = 50 μs after detonation. The spikes in the green-blue contours are consistent with development of an instability at the interface between the HE particles and the sand.

Figure 15. Sand front dispersion in the Kolsky bar direction at simulation times t = 102, 182, and 208 μs. (a) Shows the sand particle density and (b) the sand particle probability density.

Figure 16. Evolution of the particle regions (air, HE, and wet sand) during the first 500 μs after detonation. The presence of an air shock front in front of the expanding sand shell is also shown.

Figure 17. (a) The measured and (b) the simulated Kolsky bar pressure versus time after detonation. (c) Shows the measured and simulated impulse versus time response and the four regions of impulsive loading.

Figure 18. The simulated specific impulse versus time response showing the impulse contributions from the sand, air, and HE particles. The impulse and times correspond to those at the strain gauge location.

Figure 19. Wet sand and high explosive (HE) front evolution as a function of time after detonation at t = 0 s.

Figure 20. (a) Cross sectional view of the test plate sectioned through the point of maximum deflection (along X = 71.3 cm). The grey square marks on the underside of the test structure indicate the locations of picture frame support while the grey dashed lines show the location of the support structures I-beam flanges. (b) The measured and simulated deflection profile of the underside of the edge clamped plate. The vertical dashed line corresponds to the center of the plate (Y = 66 cm) which was also the position of maximum deflection.

Figure 21. A comparison of the IMPETUS predicted transient deflection of the plate at the region of maximum deflection (X = 71.3 cm; Y = 66 cm), and the experimentally measured final maximum deflection.

Figure 22. Specific impulse distribution at the plate surface after the first 1 ms of loading.

Figure 23. Effective plastic strain contours. (a) On the front and (b) the back face of test plate after it had come to rest (t = 20 ms).

Figure A1. Simulation snapshots showing the radial sand speed for simulations with and without air particles present in the simulation.

Figure A2. The maximum radial speed of the sand particles as a function of time for simulations performed with and without air particles.

Figure B1. Simulated bending and rotation of I-beam picture frame and support plate. (a) Shows the geometry prior to impact. (b) Shows the deformed structure at the time of maximum I-beam rotation (t = 2.2 ms).

Figure B2. (a) Nodal displacements for node 22570 located on rotating I-beam picture frame, node 20100 located on the support plate, and node 222 located on the 304 SS plate and (b) corresponding plot of the angle of rotation at the three nodes.

Figure B3. (a) Meshed corner of I-beam frame with effective plastic strain contours showing the region of maximum strain in the flange near the I-beam web. (b) Comparison of the effective plastic strain simulation with I-beam flange fracture location.

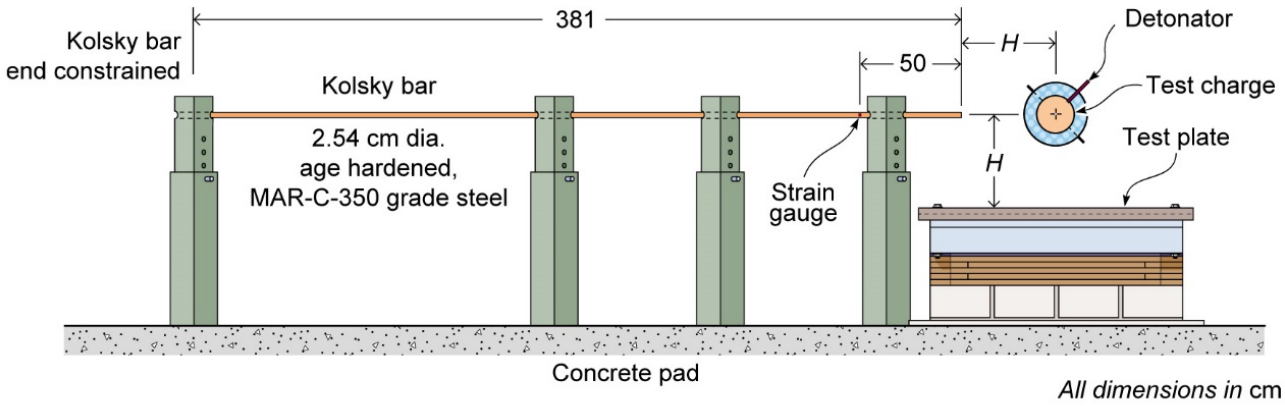

Figure 1. Schematic illustration of the test geometry. A spherical test charge was suspended a distance H over the center of an edge clamped test structure with a Kolsky bar positioned a similar distance from the center of the charge. A detonator was placed at a position that bisected the directions between the charge center and the test plate and the charge center and the Kolsky bar axis so that soil impact with the center of the plate and the face of the Kolsky bar would be similar.

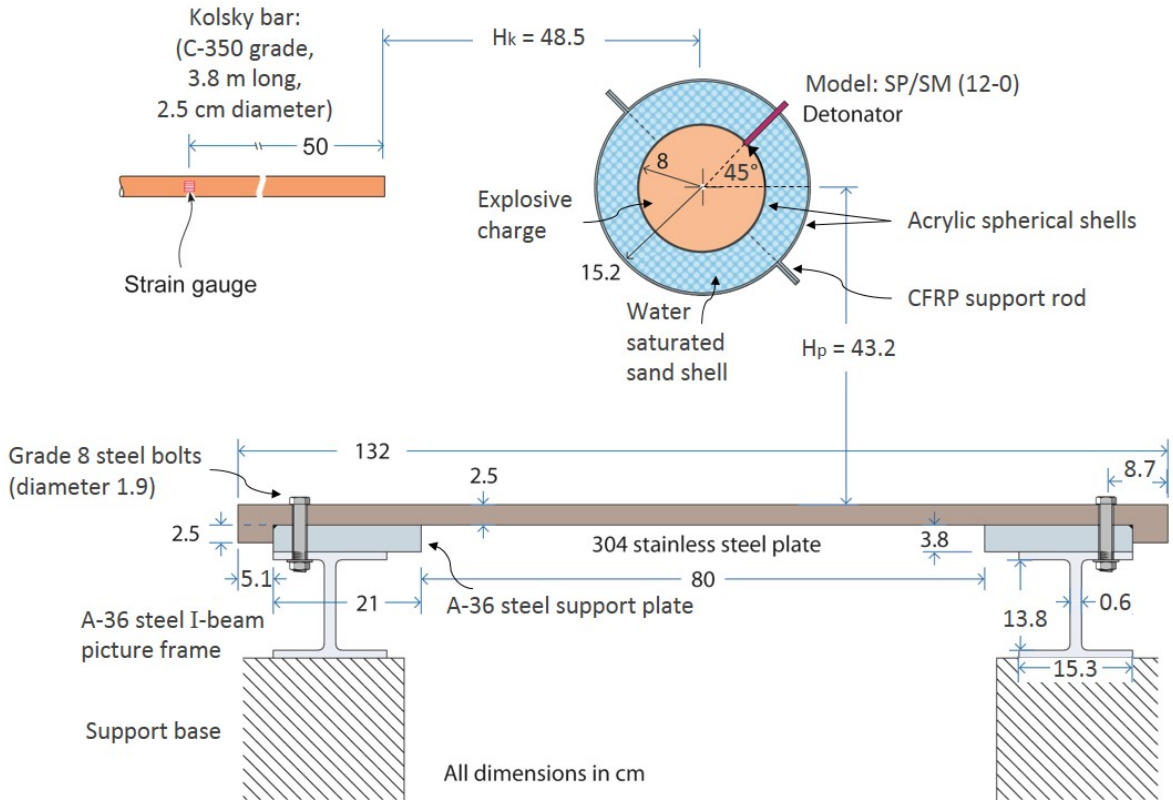

Figure 2. Schematic illustration of edge constrained test panel geometry, the location of the Kolsky bar (including its strain gauge location), the test charge geometry and the standoff distances to the Kolsky bar (H_k) and test plate (H_p) at the instant of detonation.

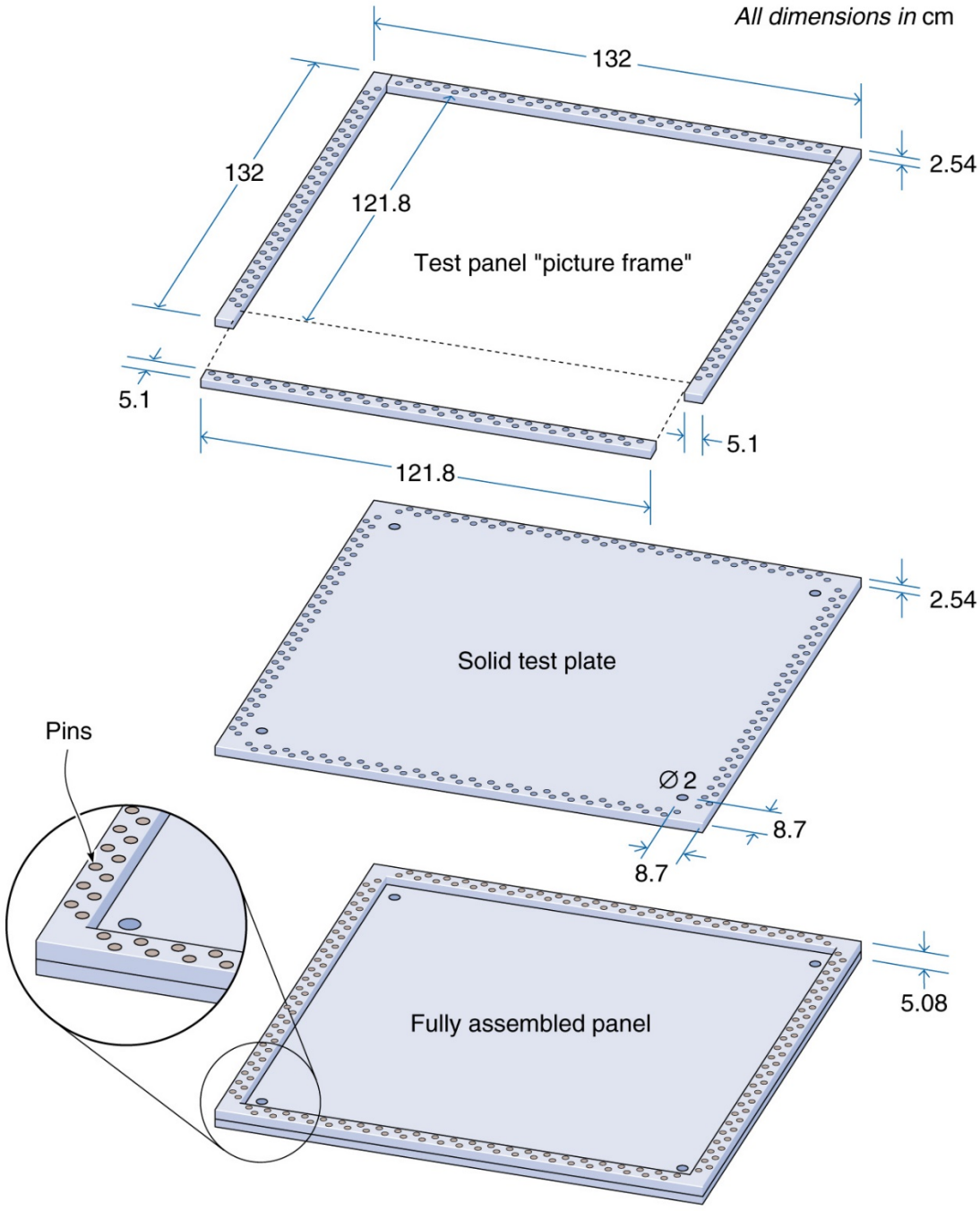

Figure 3. Construction of the test plate with the welded frame used for attachment to the test stand. Steel dowel pins were press fitted to strengthen the welded connection between the test plate and the four rectangular bars.

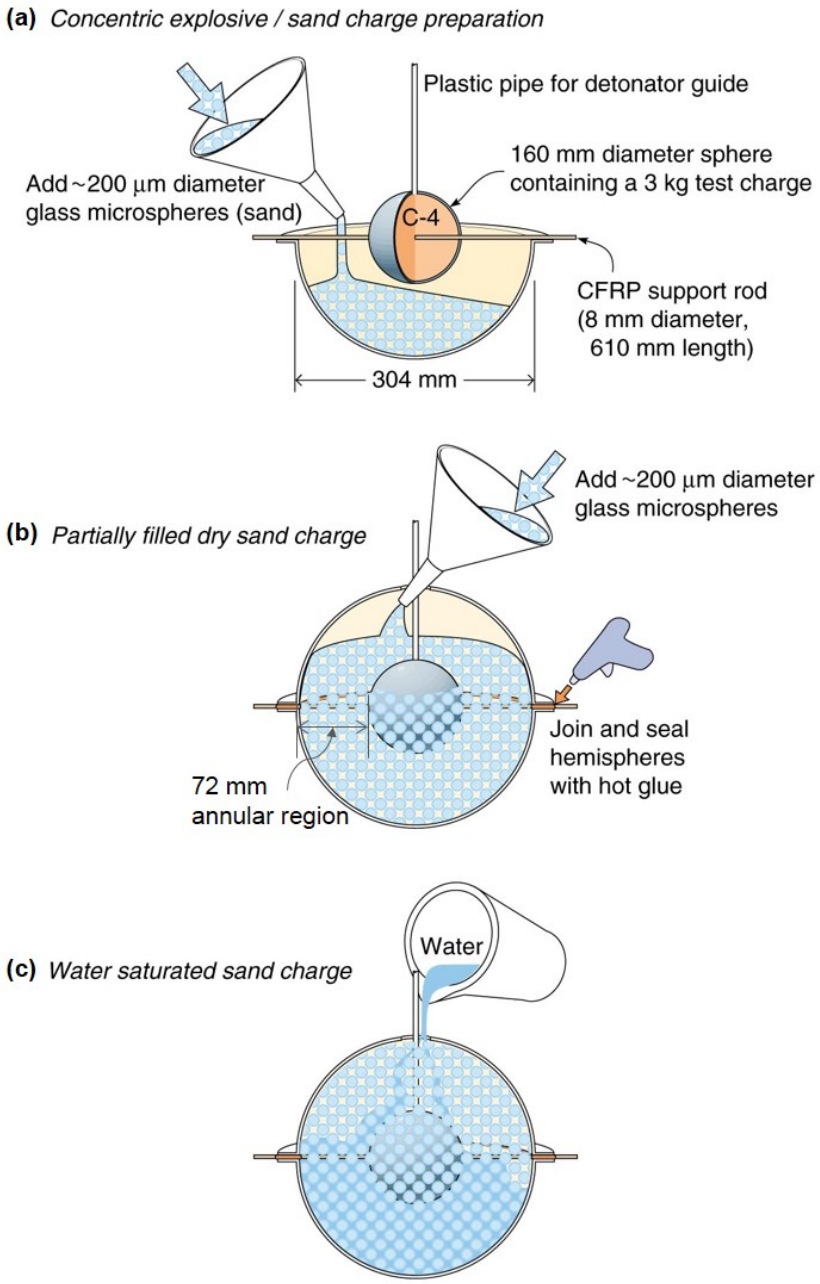

Figure 4. The geometry and procedure used to assemble the spherical test charge with its concentric shell of water-saturated synthetic sand.

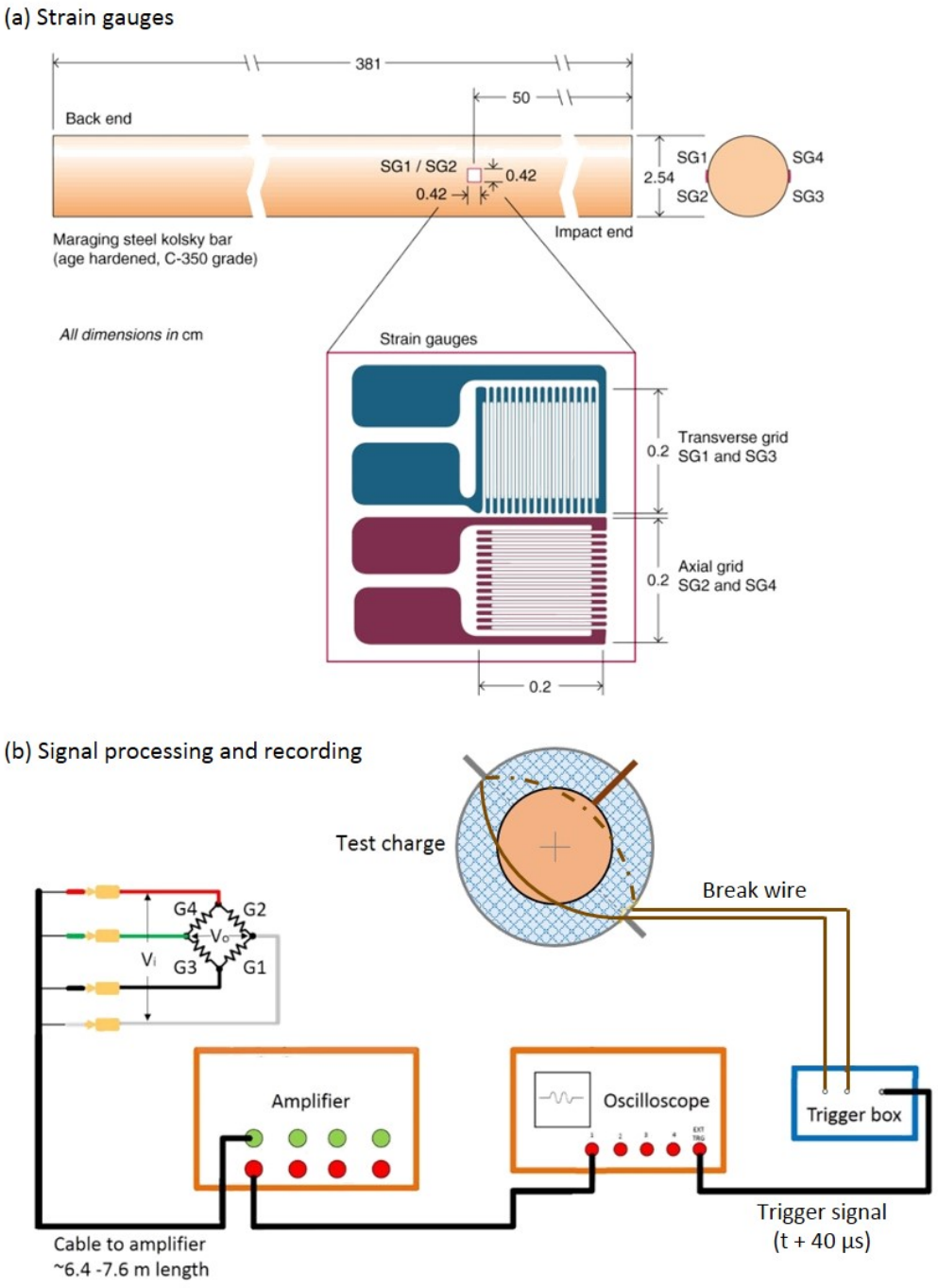

Figure 5. (a) The strain gauge sensor arrangement for the instrumented Kolsky bar. (b) Shows the signal conditioning and digital data recording arrangement. The trigger signal used to begin digital data recording was initiated by rupture of a break wire attached to the outer shell of the test charge. This trigger event was initiated 40 μs after the start of the detonation process.

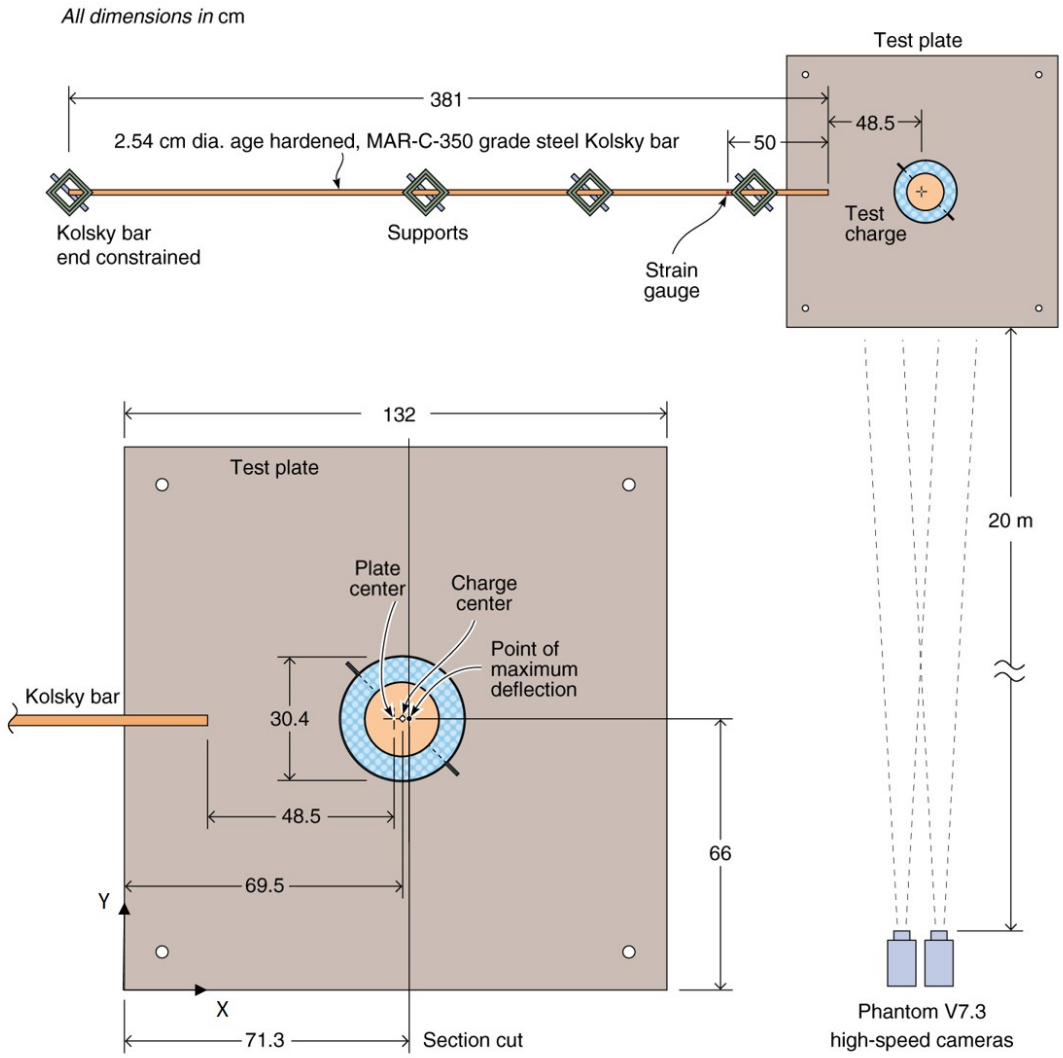

Figure 6. Plan view of the X-Y plane showing camera locations. An expanded view of the test charge and plate shows the plate center, the charge center at detonation, and the point of maxiumum plate deflection (X = 71.3 cm and Y = 66.0 cm) after the event. The location of the section cut used to obtain a plate deflection profile is also shown. The origin of the coordinate system used for the study was at the front (lower) left corner of the test plate.

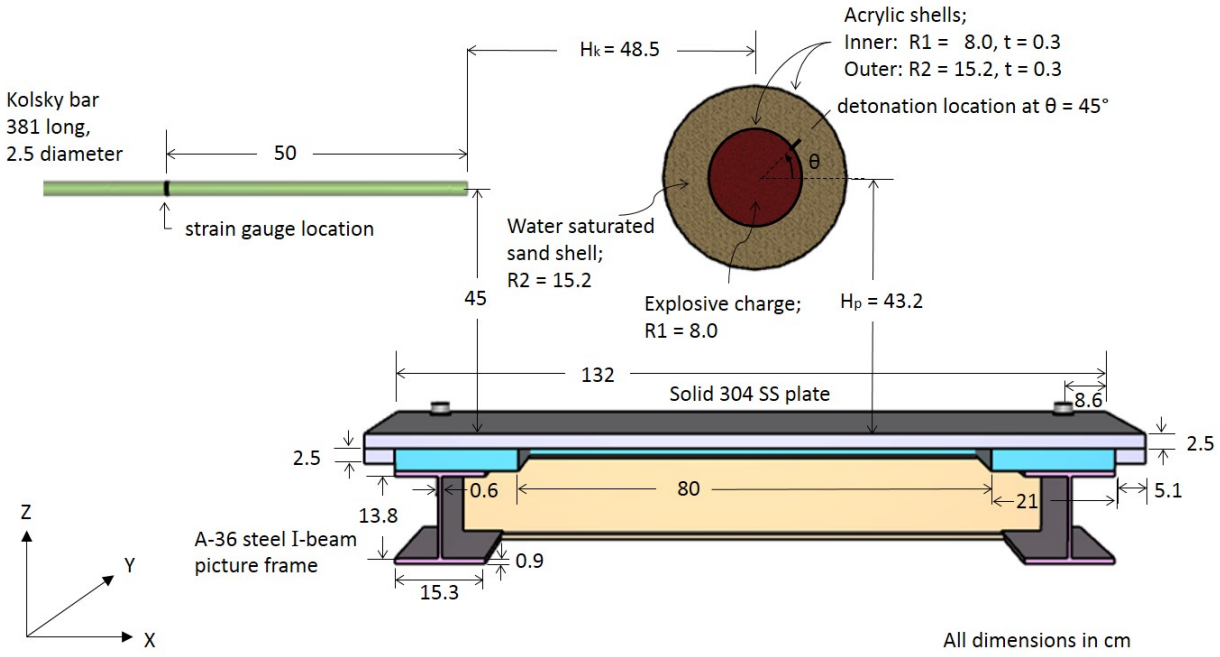

Figure 7. A cross-section through the mid-plane of the FE model geometry used for the Afea discrete particle based simulation. The coordinate axis origin was located at the front left corner of the top of the test plate (out of the plane of this figure) as shown in Figure *6*.

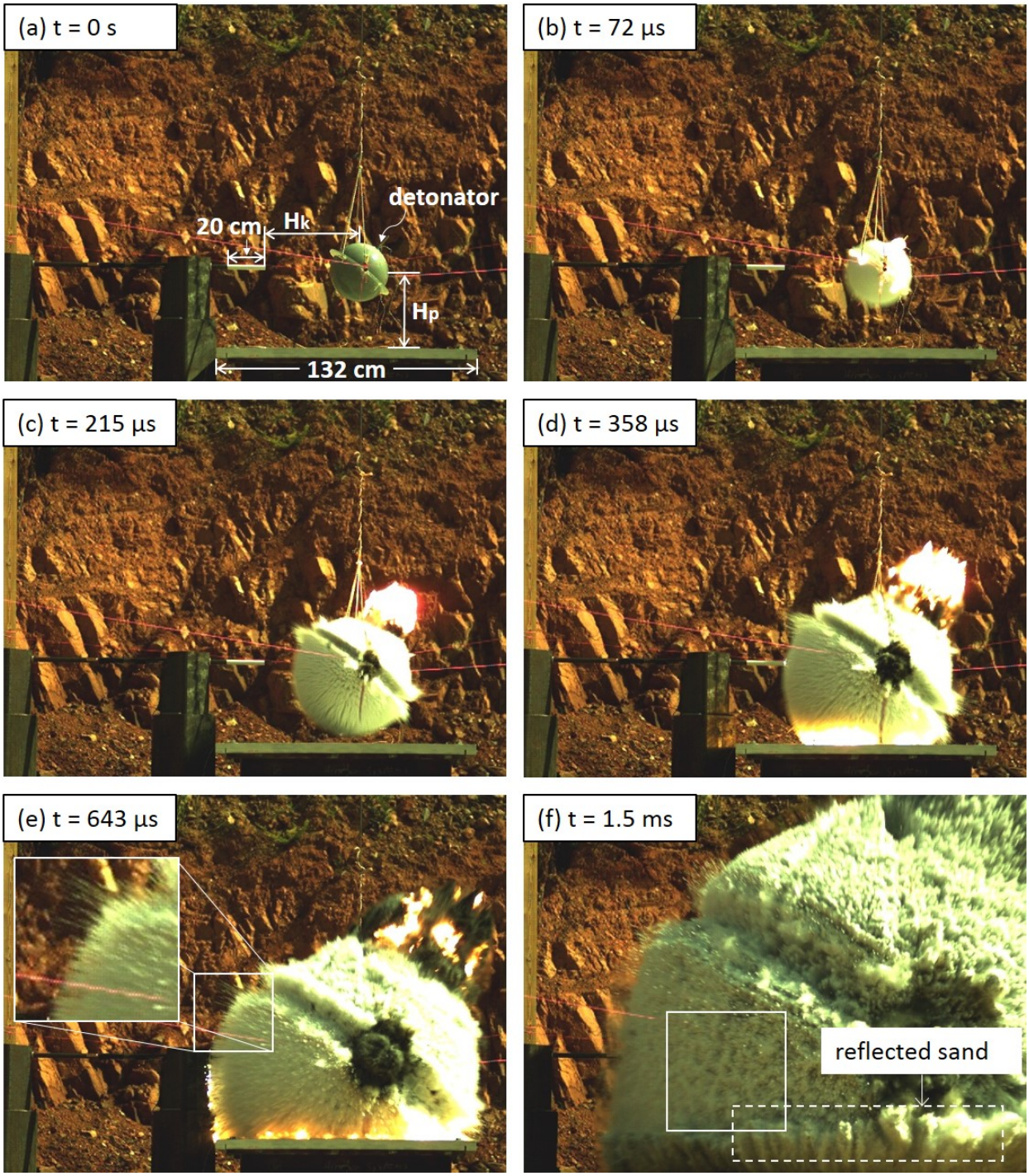

Figure 8. Sand front propagation observed with the wide-angle video camera; (a) t = 0 s (instant of detonation), (b) t = 72 µs (c) t = 215 µs, (d) t = 358 µs, (e) t = 643 µs, (f) = 1.5 ms. The distance from charge center to the test plate, H_p = 43.2 cm and to the Kolsky bar, H_k = 48.5 cm. (e) Shows a magnified region of the outermost sand front showing the presence of sand spikes (fingers). The white box in (f) indicates the region observed in Figure 10.

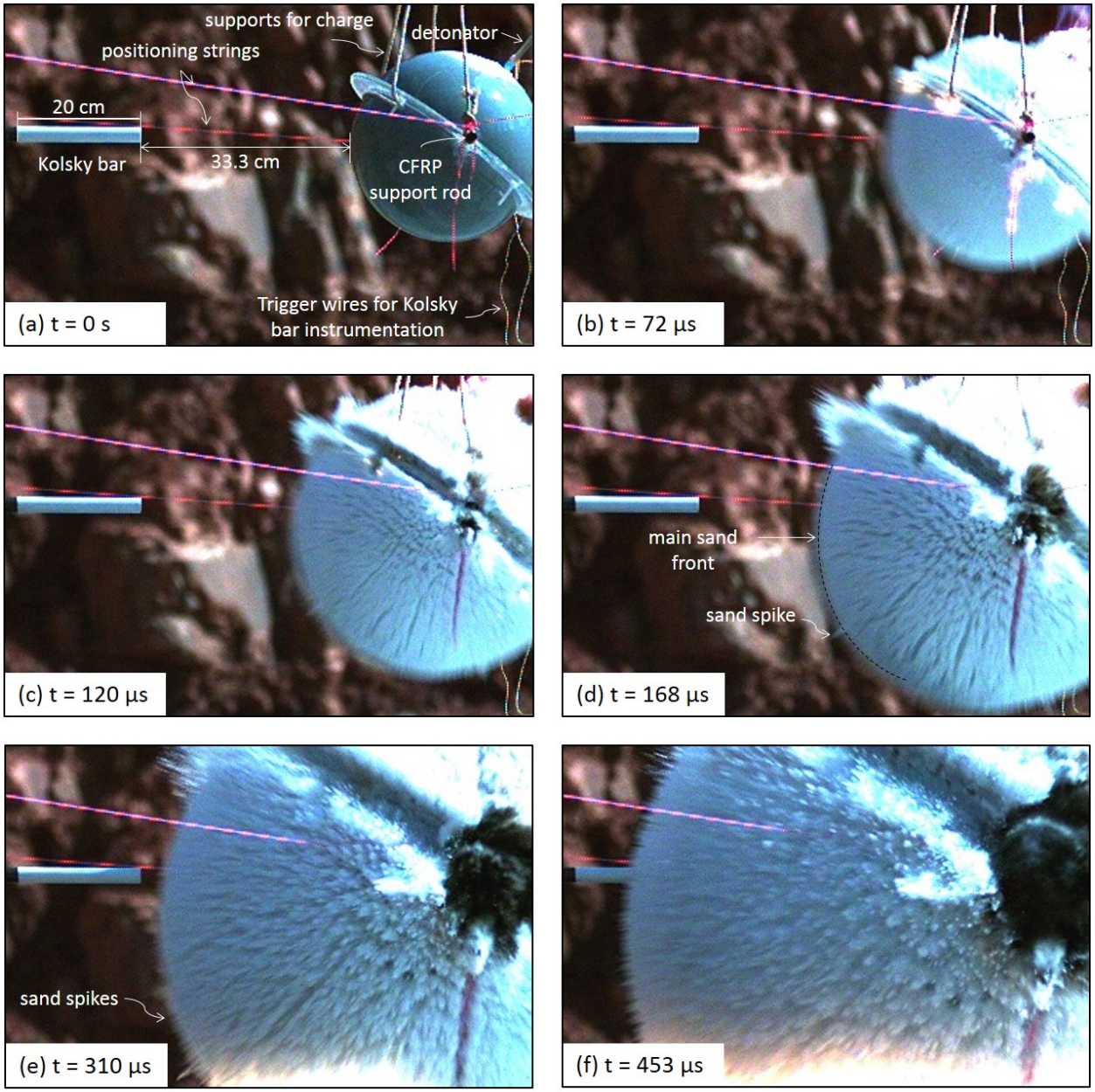

Figure 9. Images of the sand using the higher spatial resolution high speed camera at times (a) t = 0 s (instant of detonation), (b) t = 72 µs, (c) t = 120 µs, (d) t = 168 µs, (e) t = 310 µs, and (f) = 453 µs. The sand progression towards the Kolsky bar, the main sand front expansion, and the sand fingering effect can be seen in (d).

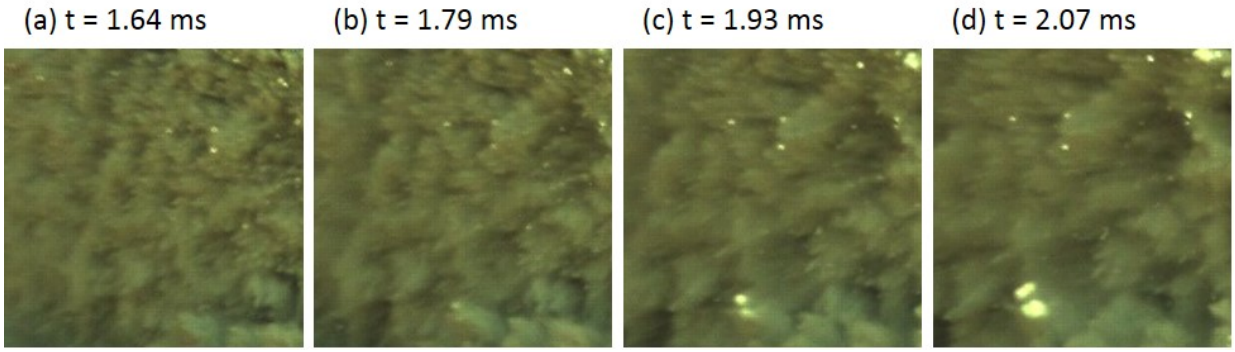

Figure 10. Expanded square region of sand front expansion from the white box region in Figure 8(f). The sand front consisted of many circumferentially expanding conical regions. As propagation of the front advanced, the cones evolved into arrays of smaller diameter expanding cones.

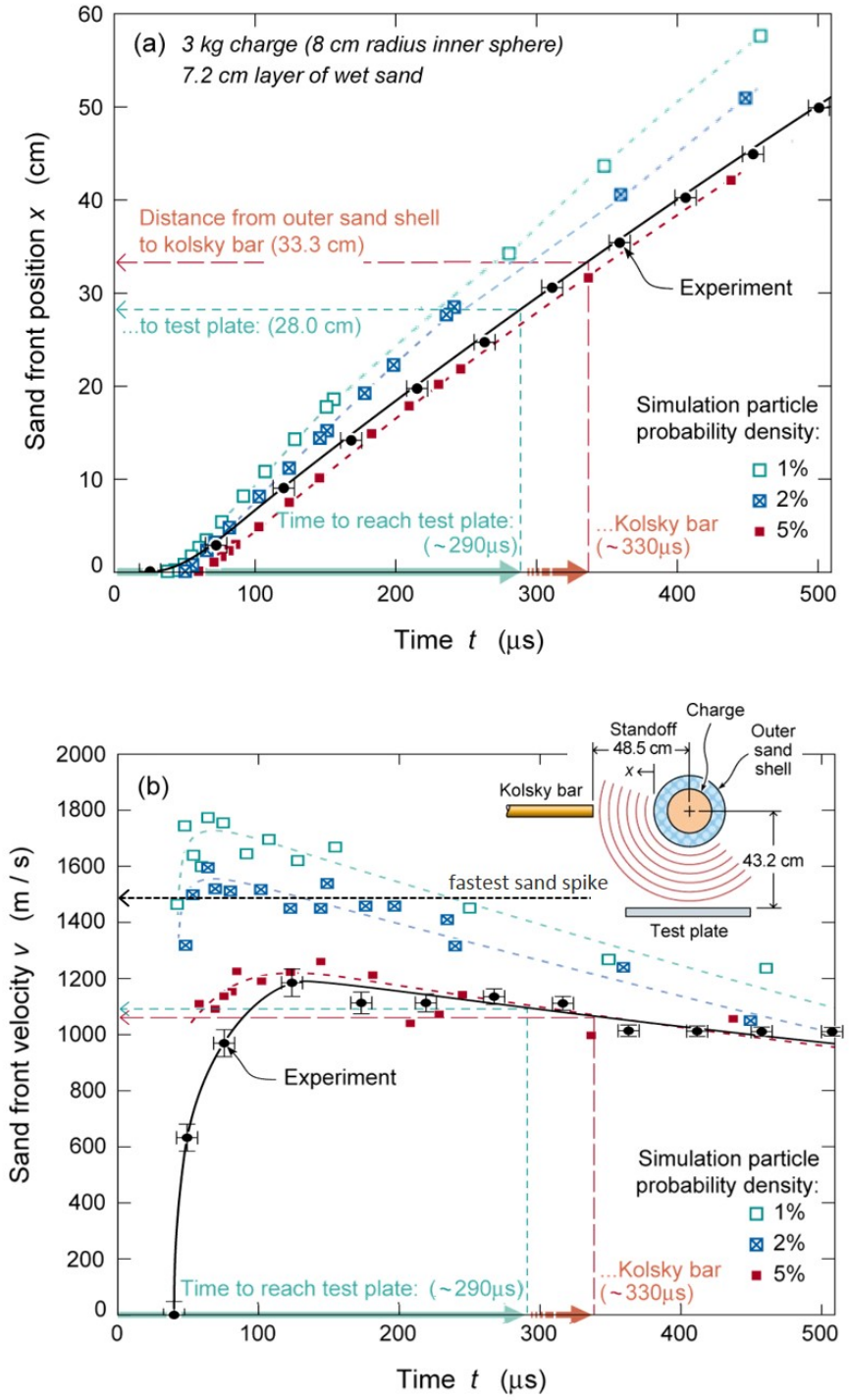

Figure 11. (a) Experimental and IMPETUS Afea predicted sand front positions measured in the Kolsky bar direction (horizontal X direction) and (b) sand front velocity vs time after detonation. The velocity of the fastest experimentally observable sand spike (finger) is also indicated on (b). The estimated time for the sand to reach both the Kolsky bar and test plate are also shown.

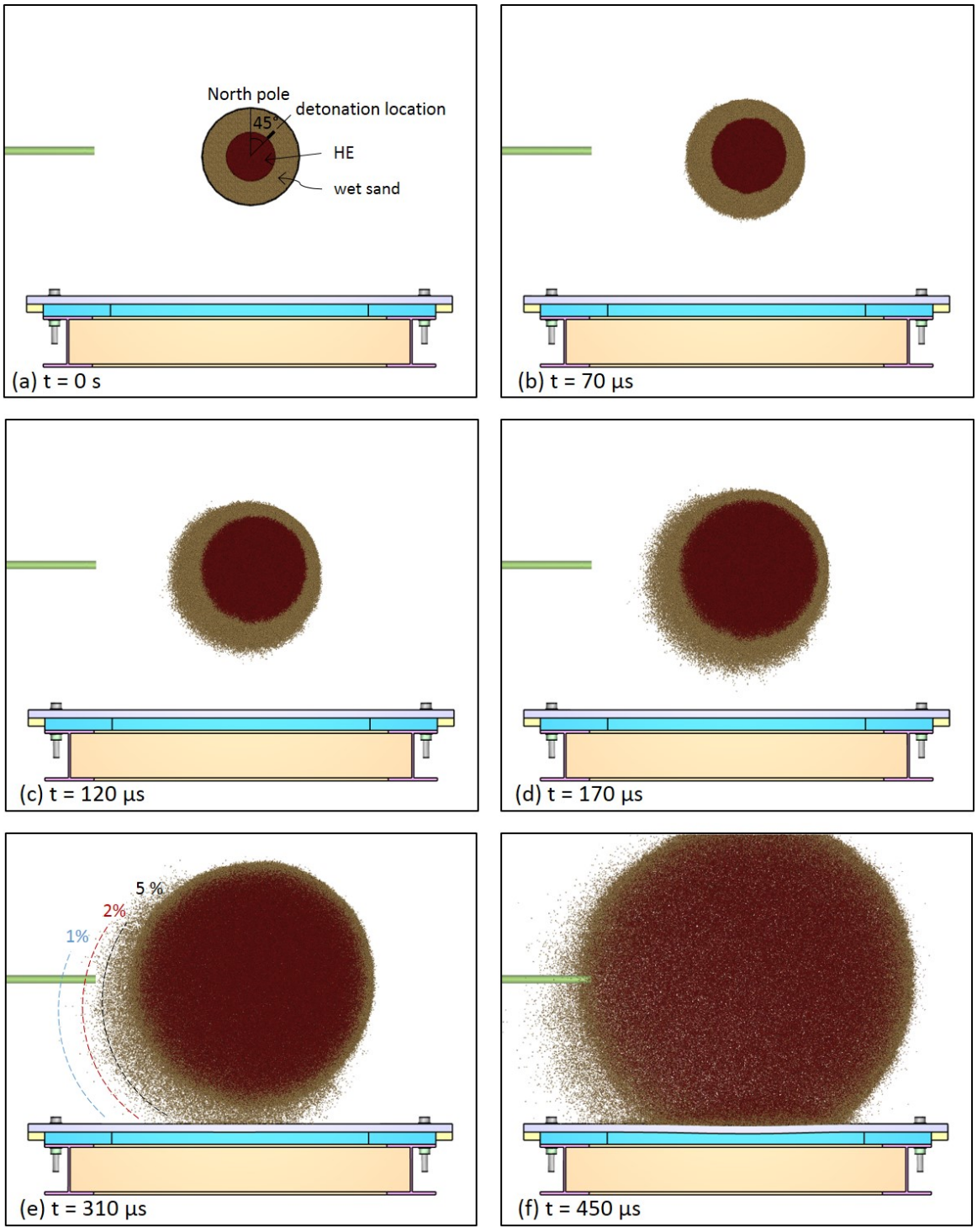

Figure 12. IMPETUS Afea predicted (tan colored) sand front positions. (a) Corresponds to the instant of detonation (t = 0 s). The position of the (red) HE particles is also shown, but air particles are hidden to improve visualization of sand and HE particle locations. Sand particle probability density contours are identified in (e) showing that low volume fraction of high-speed sand had travelled much further than the main sand front.

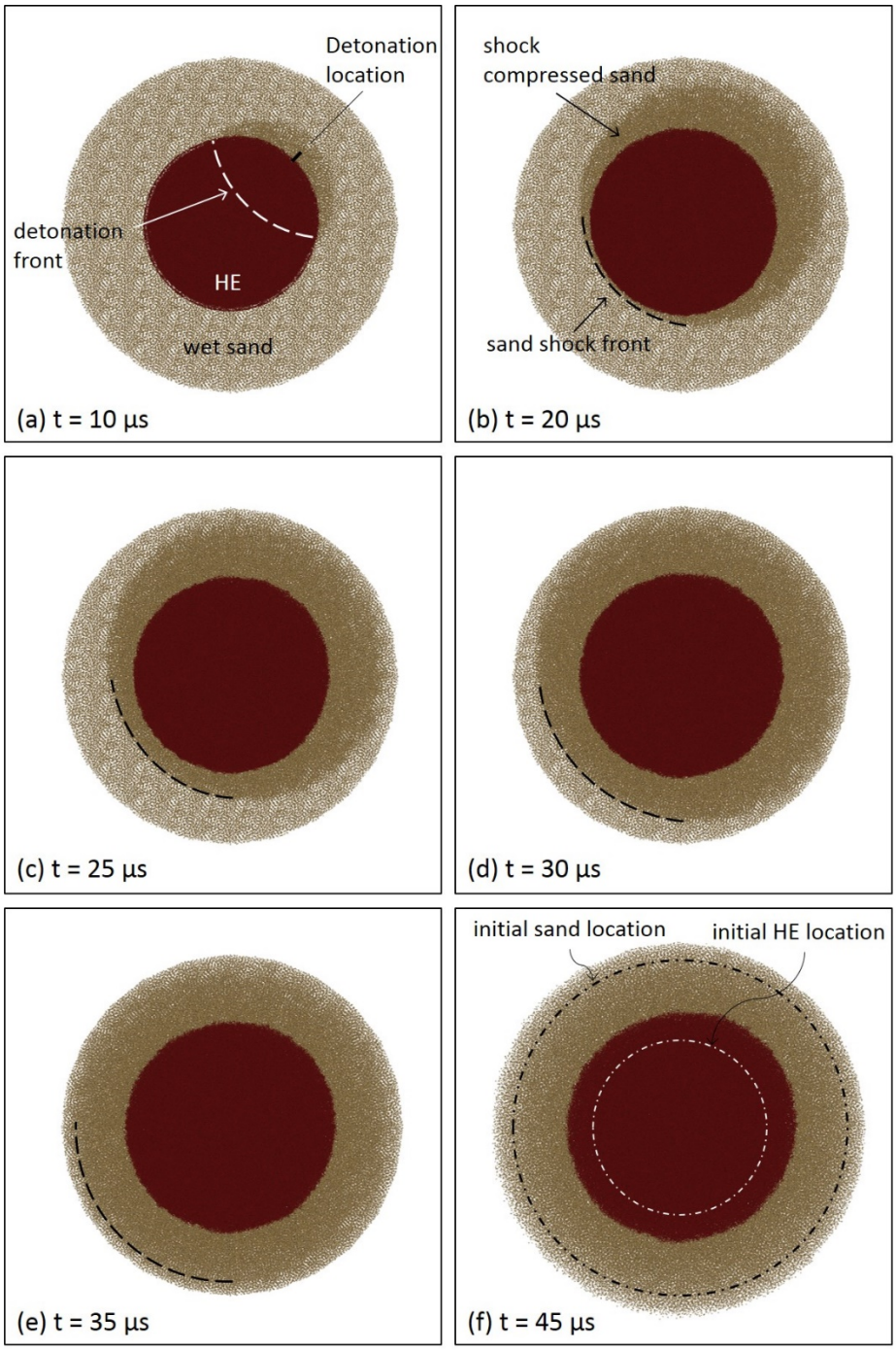

Figure 13. A simulation sequence following detonation of the test charge. The propagation of a detonation front through the HE and the locations of compressive shock front within the annular wet sand shell are also shown. (f) Shows the distance the sand and HE particles were displaced from their initial locations at t = 45 µs after initiation of detonation.

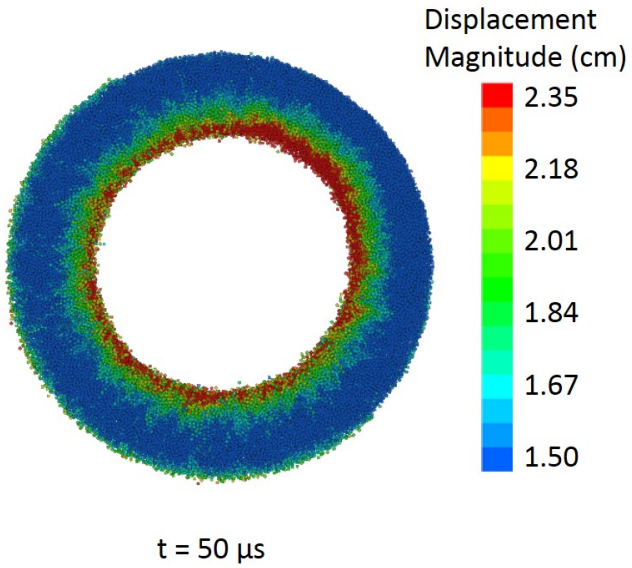

Figure 14. Sand particle shell with color contours corresponding to the magnitude of the particle displacement at t = 50 µs after detonation. The spikes in the green-blue contours are consistent with development of an instability at the interface between HE particles and the sand.

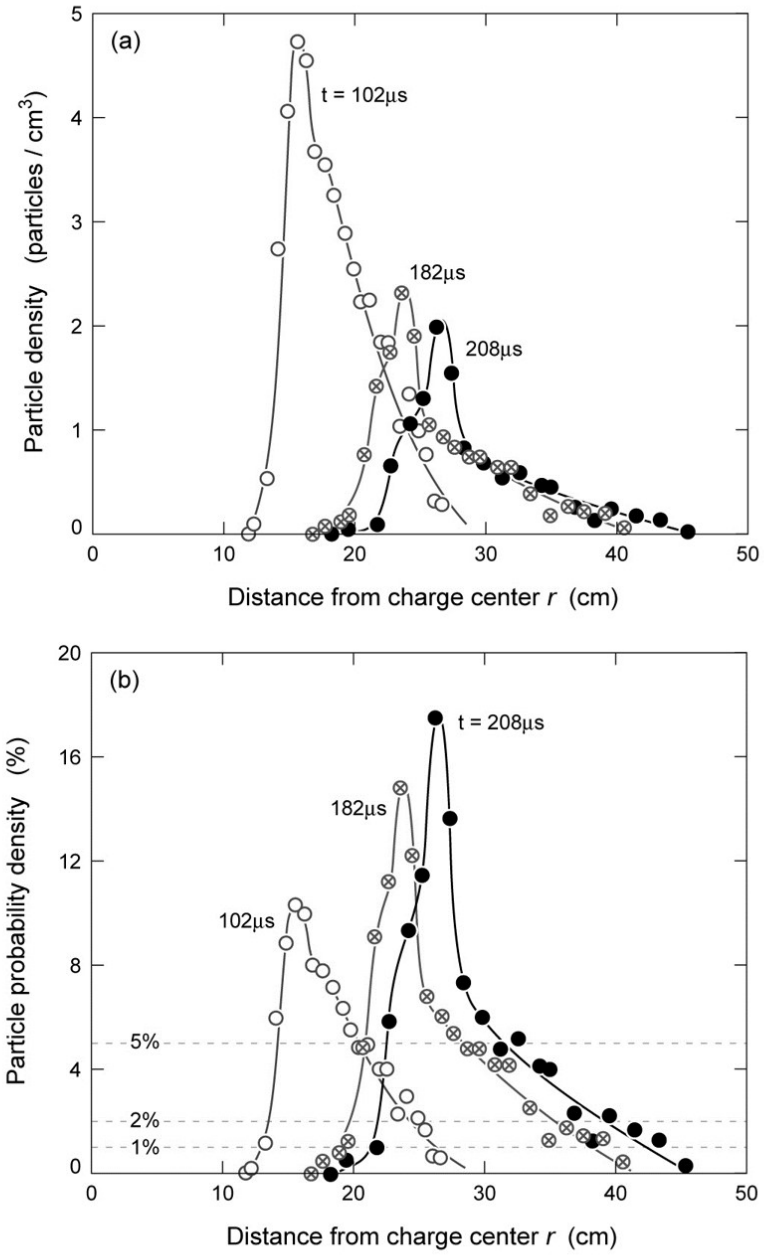

Figure 15. (a) The variation in sand particle density and (b) the sand particle probability density as a function of distance from the charge center (measured in the Kolsky bar direction) at simulation times t = 102, 182, and 208 μs.

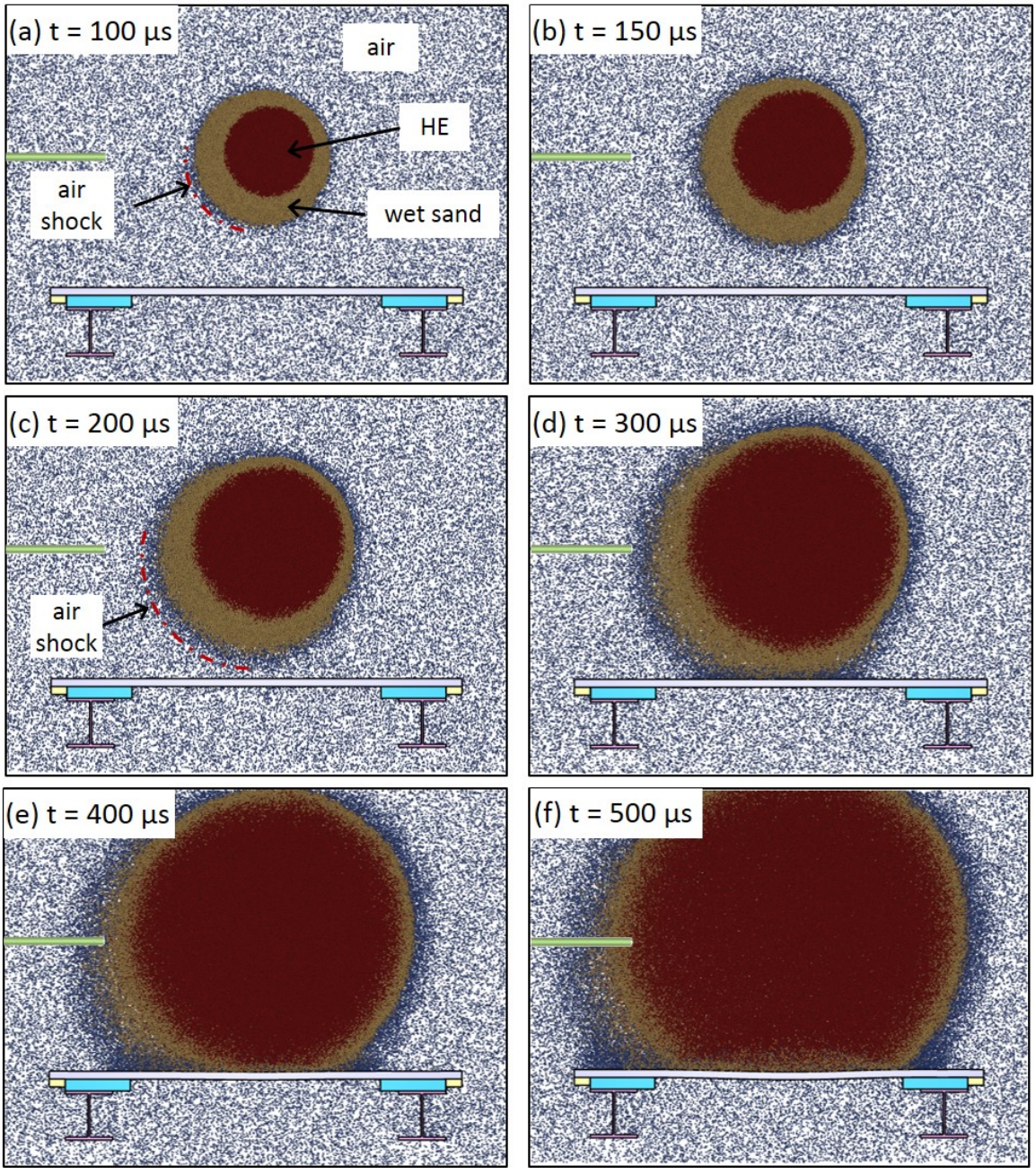

Figure 16. Evolution of the air, HE, and wet sand particle regions during the first 500 µs following detonation. The presence of an air shock (darker blue) in front of the expanding sand shell can be seen.

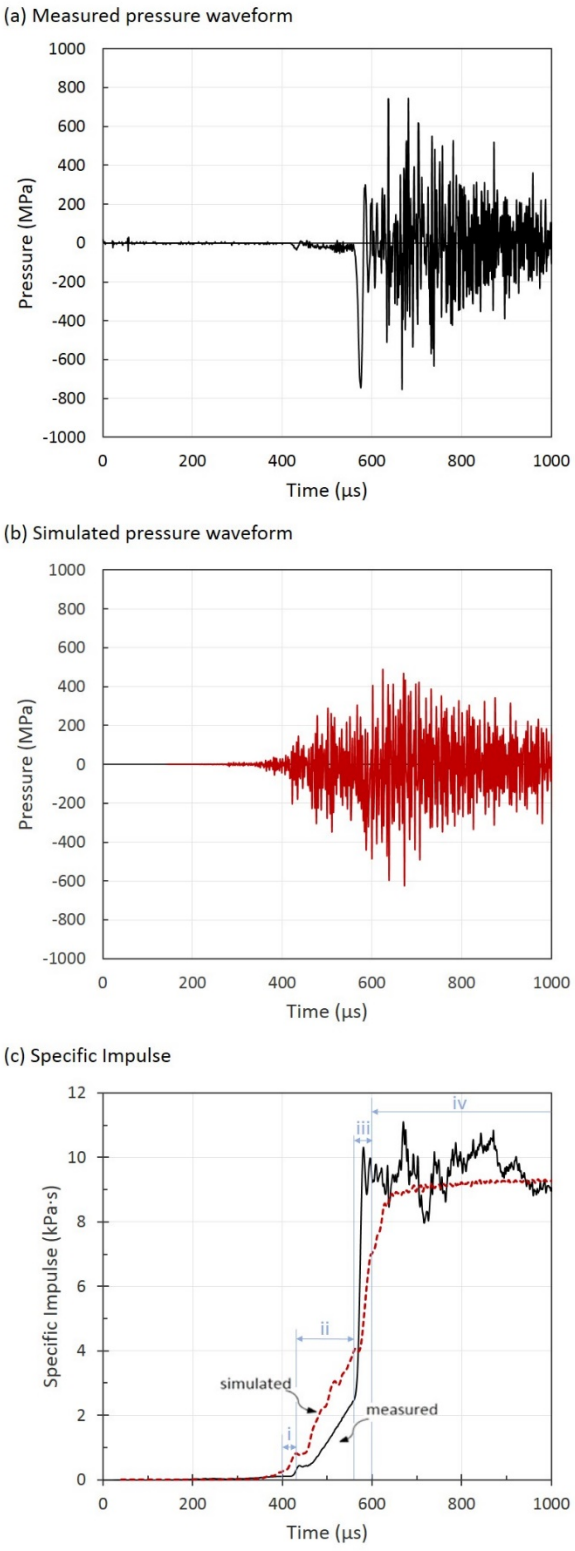

Figure 17. (a) The measured and (b) simulated Kolsky bar pressure versus time after detonation. (c) Shows the measured and simulated impulse versus time response and the four regions of impulsive loading.

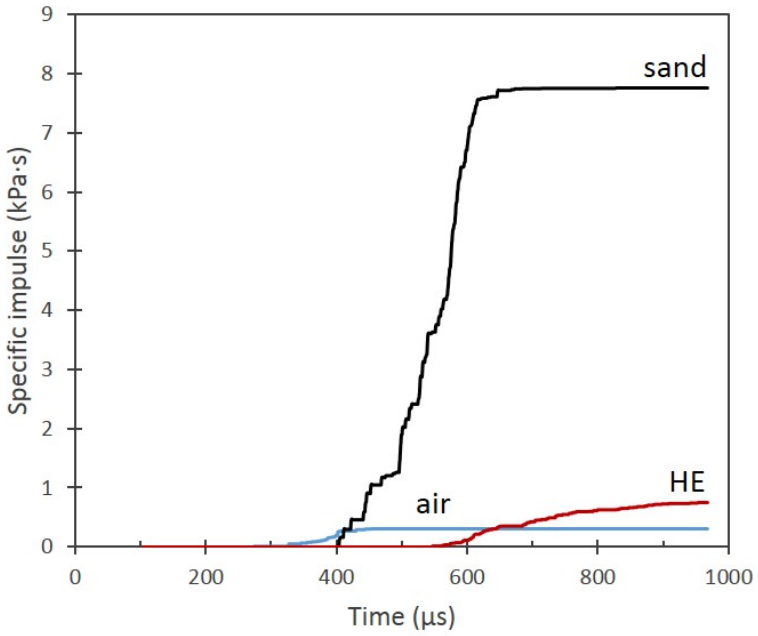

Figure 18. The simulated specific impulse contributions from the sand, air, and HE particles versus time at the strain gauge location.

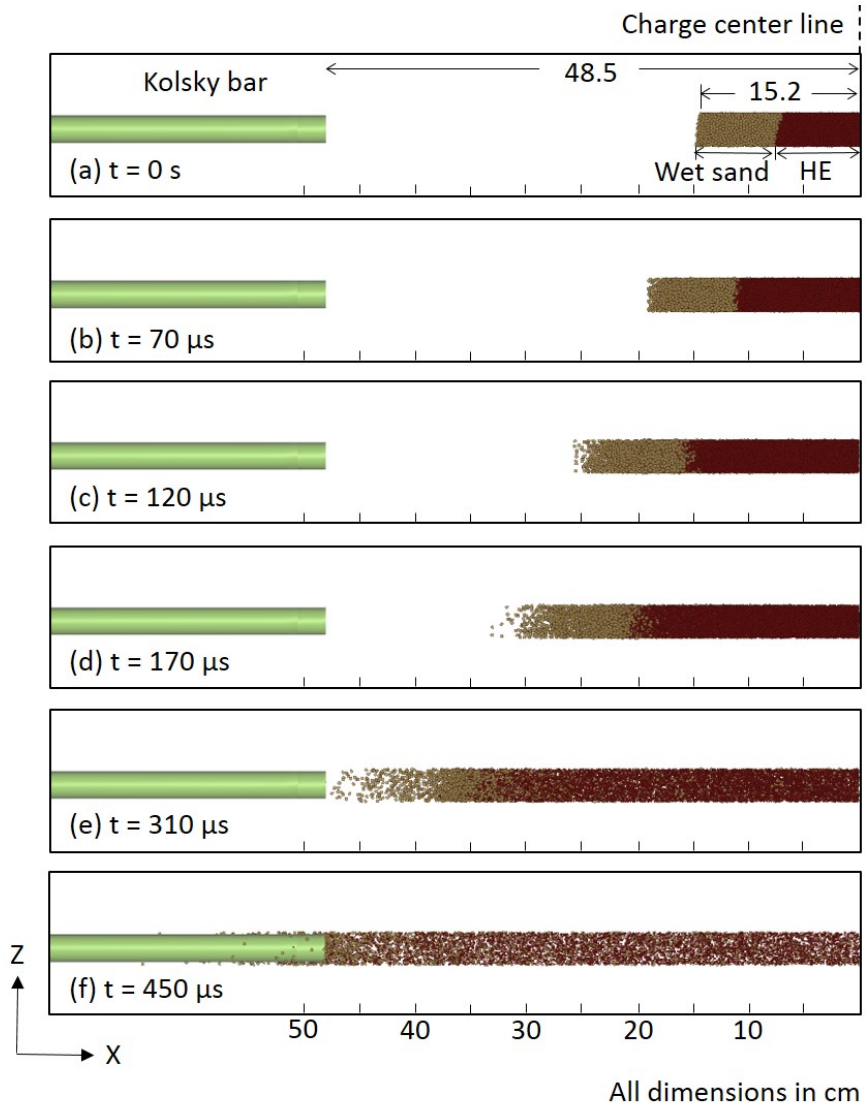

Figure 19. The position of sand and high explosive (HE) particles that impacted the Kolsky bar at selected times after detonation (at t = 0 s).

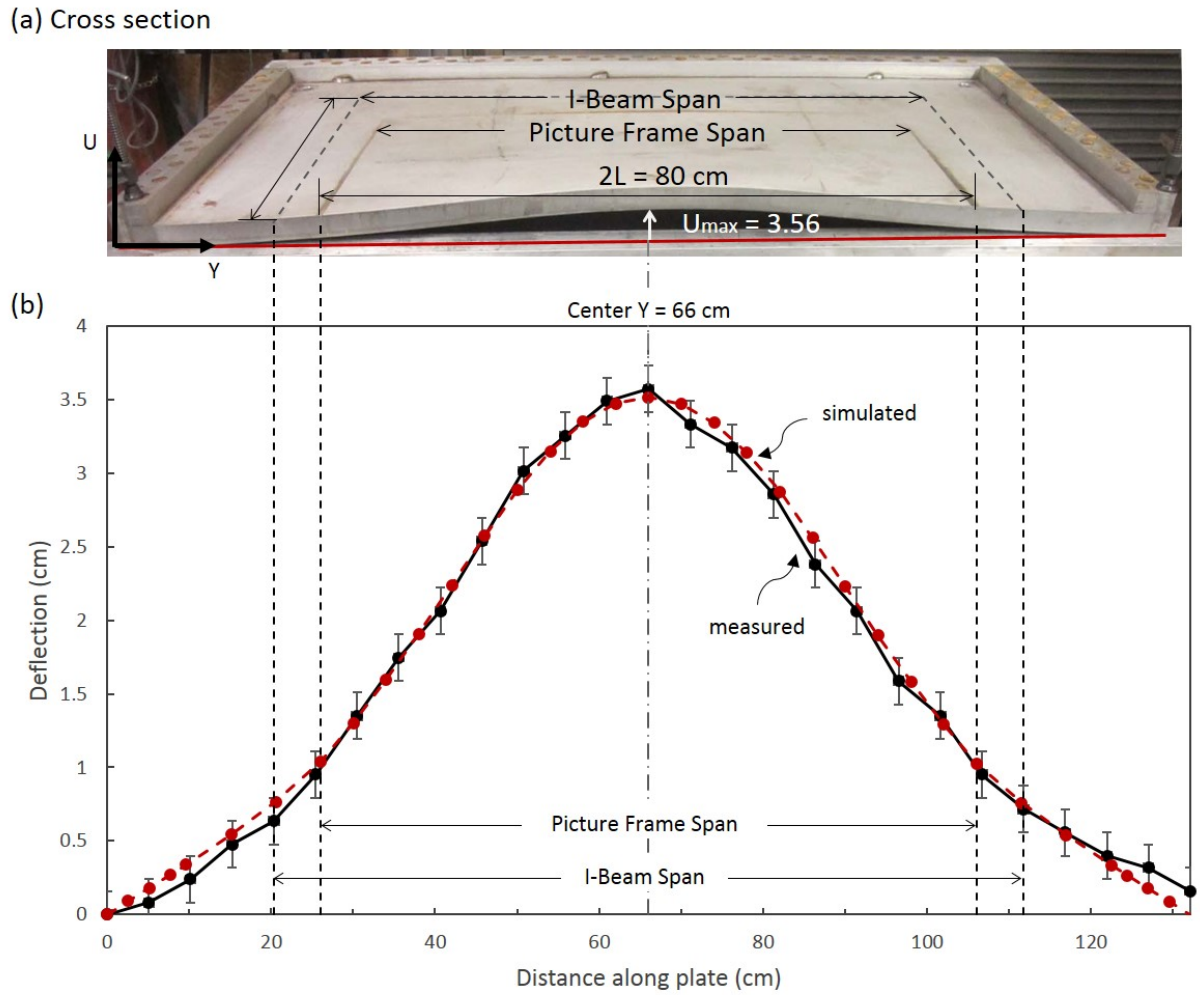

Figure 20. (a) Cross sectional view of the test plate sectioned through the point of maximum deflection (along X = 71.3 cm). The grey square marks on the underside of the test structure indicate the locations of the picture frame support while the grey dashed lines show the location of the I-beam flanges of the support structure. (b) The measured and simulated deflection profile of the underside of the edge clamped plate. The vertical dashed line corresponds to the center of the plate in the Y-direction (at Y = 66 cm) which was also the position of maximum deflection.

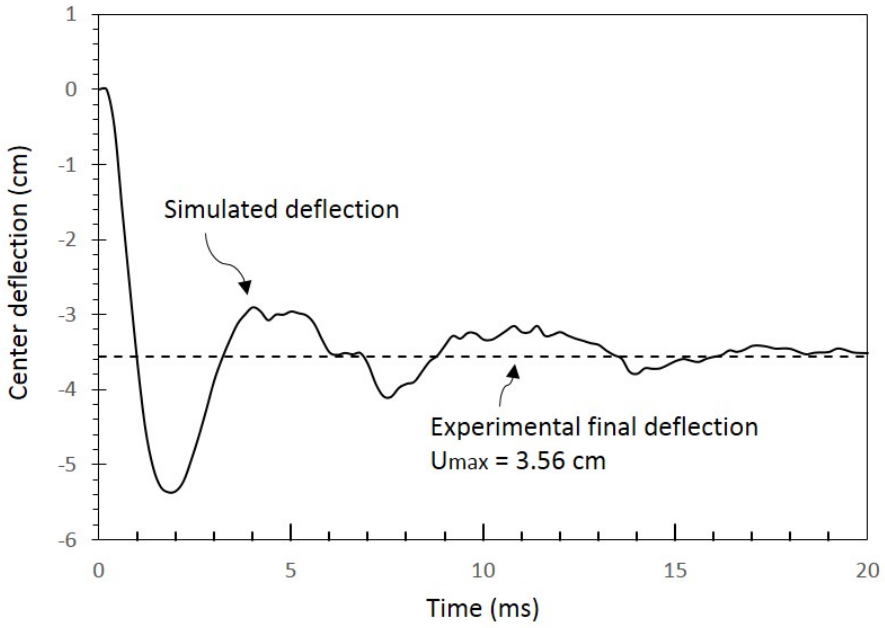

Figure 21. A comparison of the IMPETUS predicted transient deflection of the plate at the region of maximum deflection (X = 71.3 cm; Y = 66 cm), and the experimentally measured final maximum deflection.

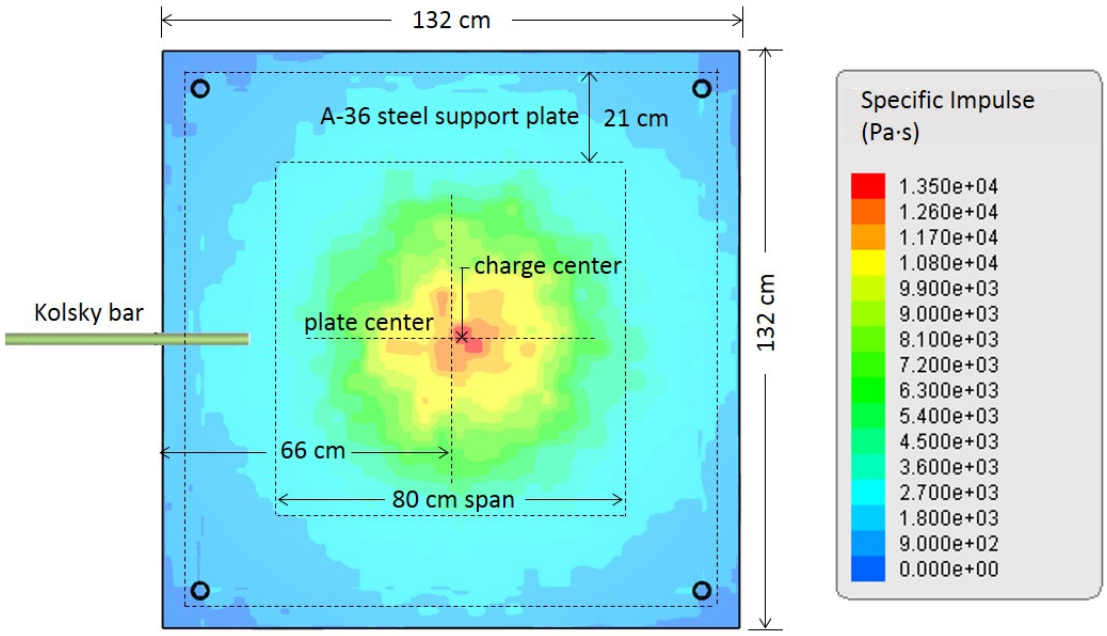

Figure 22. Specific impulse distribution at the plate surface after the first 1 ms of loading.

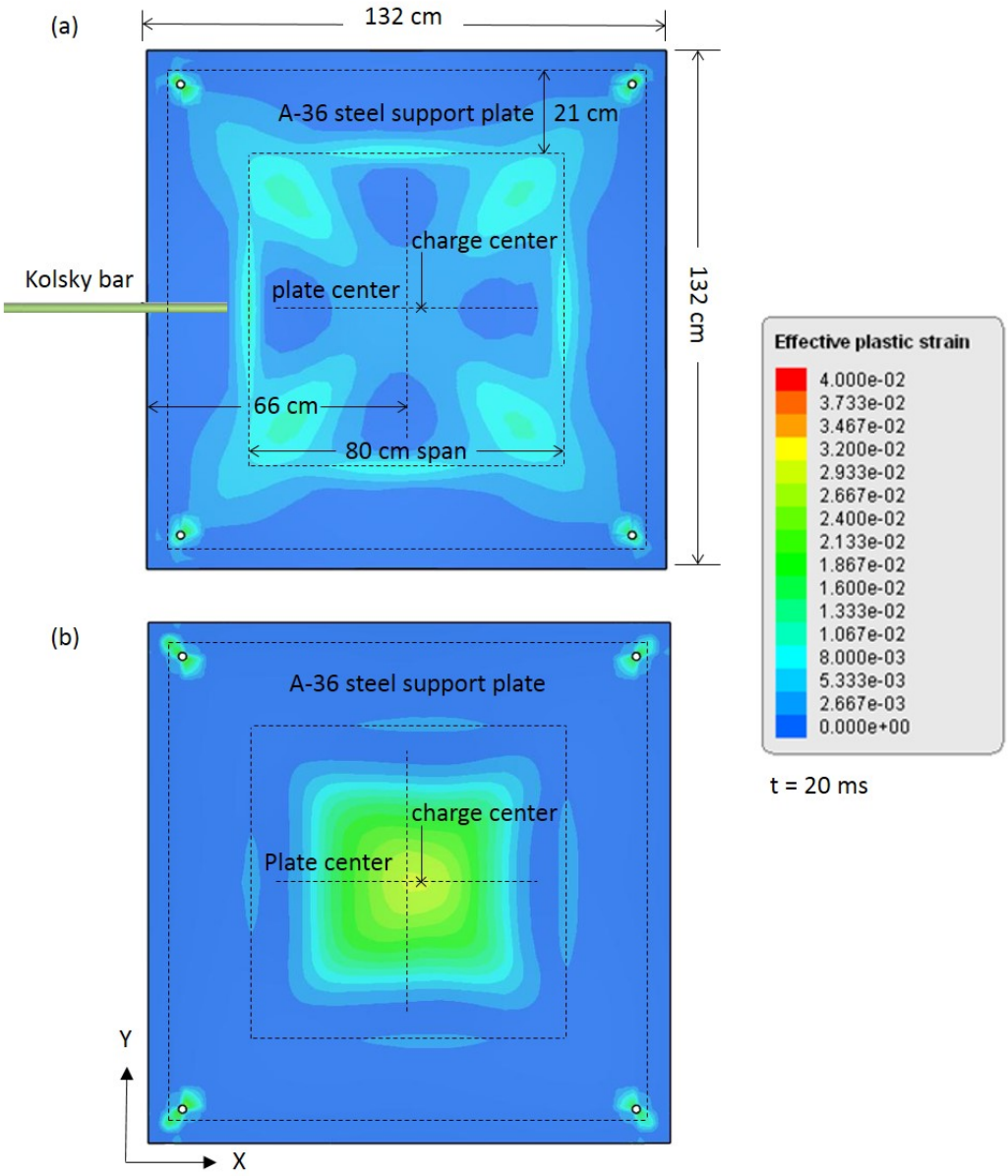

Figure 23. Effective plastic strain contours of the test plate. (a) On the front and (b) the back face of test plate after it had ceased reverberation (t = 20 ms).

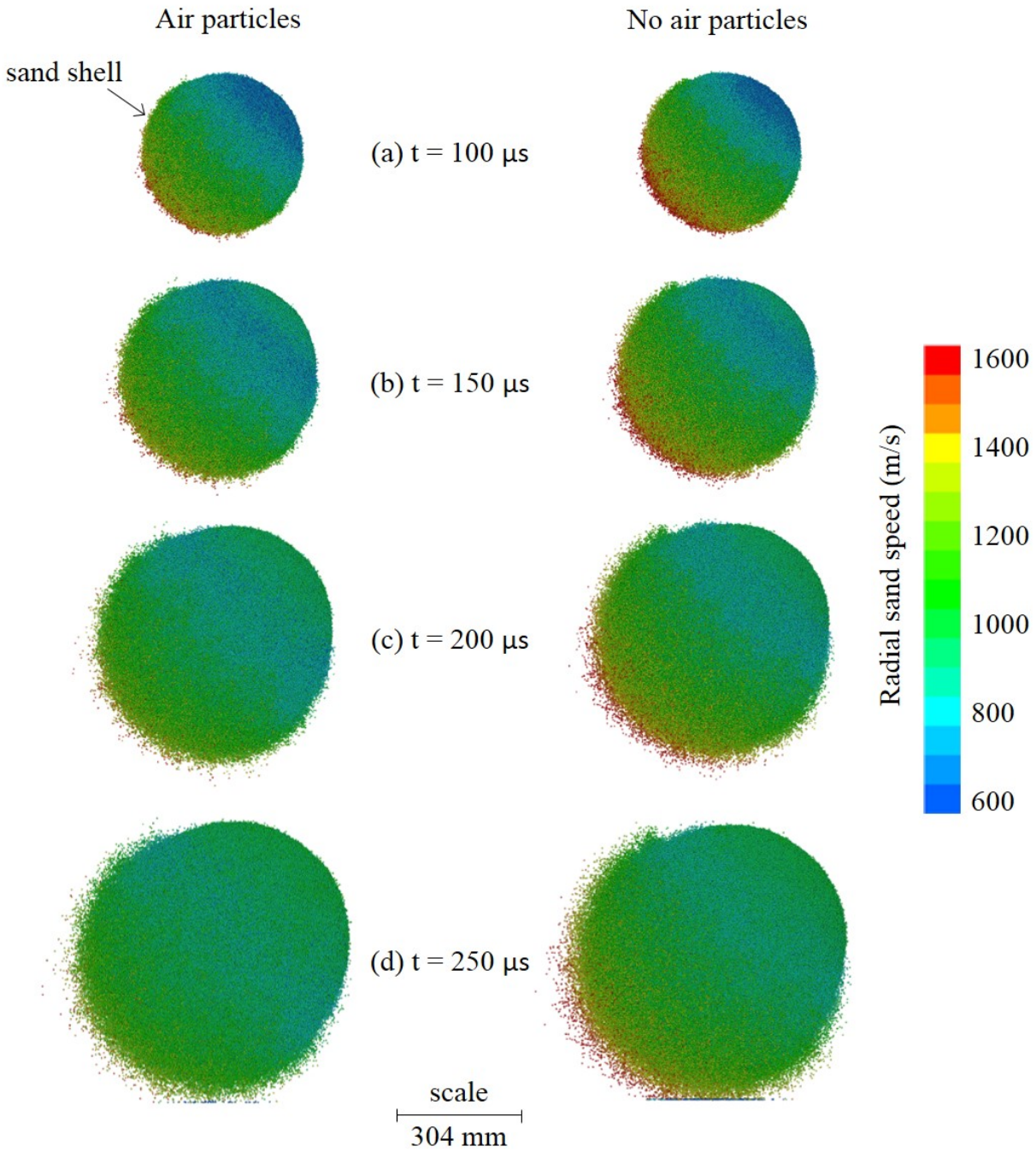

Figure A1. Simulation snapshots indicating the radial sand particle speeds for simulations with and without air particles present in the simulation. The presence of air particles significantly reduced the speed of the leading edge sand particles.

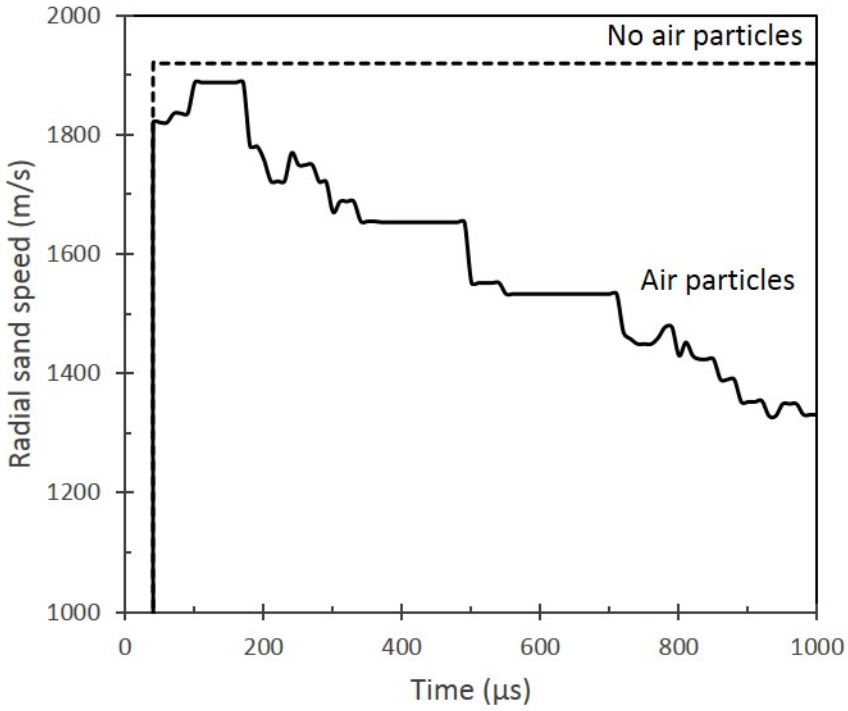

Figure A2. The maximum radial speed of sand particles as a function of time for simulations performed with and without air particles.

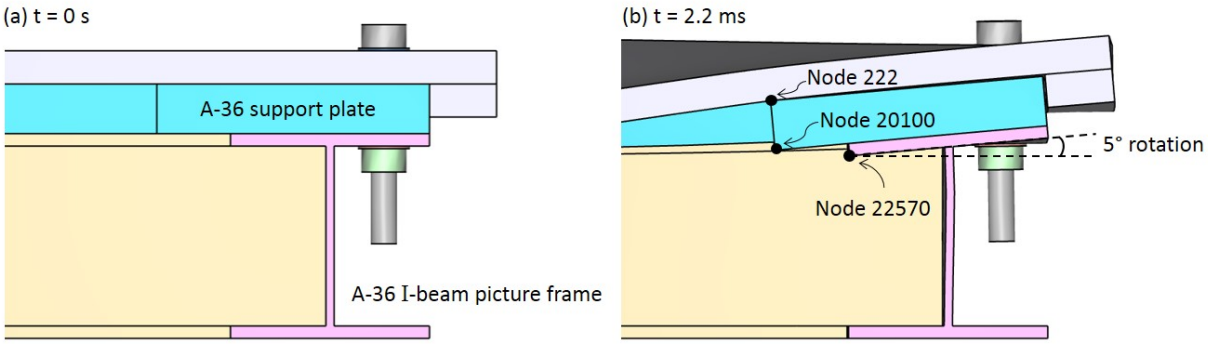

Figure B1. Simulated bending and rotation of I-beam picture frame and support plate. (a) Shows the geometry prior to sand impact. (b) Shows the deformed structure at the time of maximum I-beam rotation (t = 2.2 ms).

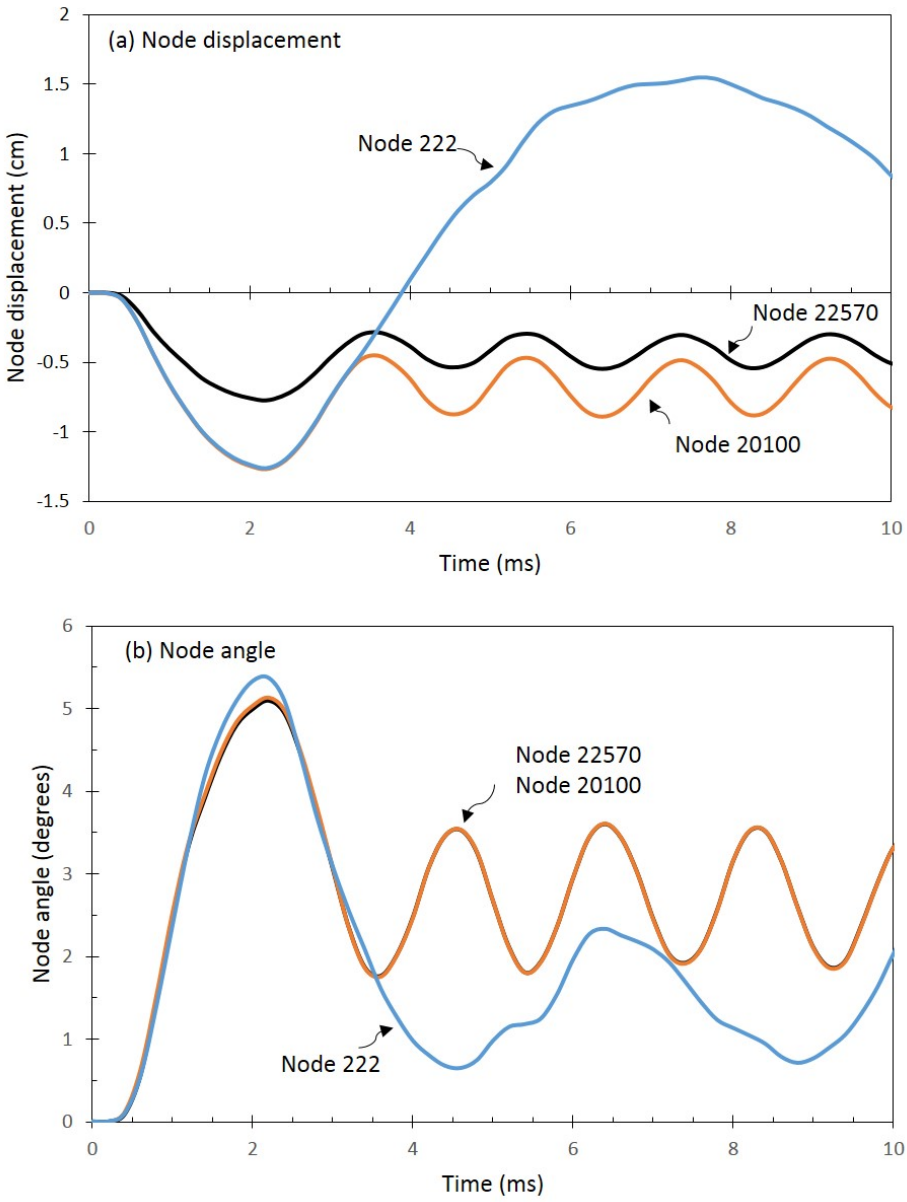

Figure B2. (a) Nodal displacements for node 22570 located on rotating I-beam picture frame, node 20100 located on the support plate, and node 222 located on the 304 SS plate and (b) corresponding plot of the angle of rotation at the three nodes.

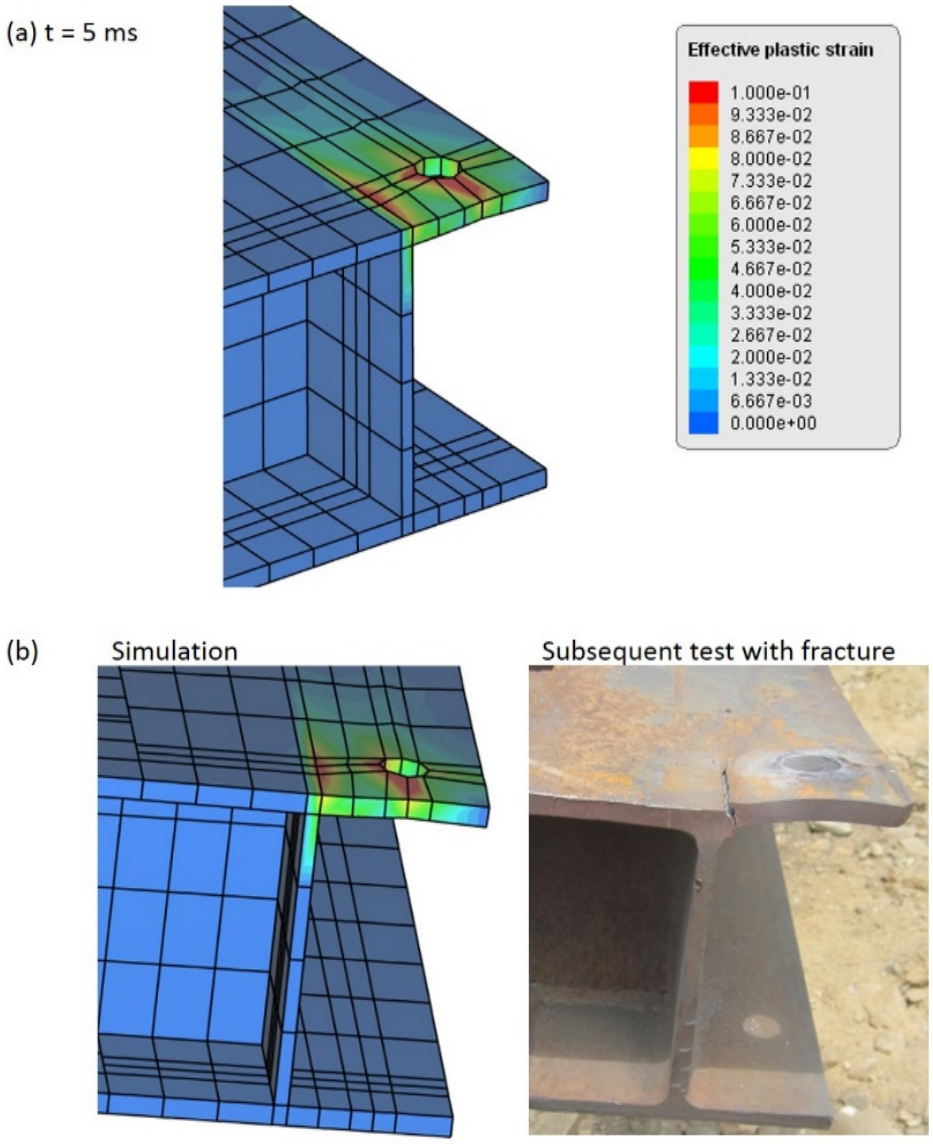

Figure B3. (a) Meshed corner of I-beam frame with effective plastic strain contours showing the region of maximum strain in the flange near the I-beam web-flange transition. (b) Comparison of the effective plastic strain simulation with I-beam deformation and fracture location.